Article

Robust Super-Twisting Sliding Mode Backstepping Control Blended with Tracking Differentiator and Nonlinear Disturbance Observer for an Unknown UAV System

Sungbum Park [1] and Seongik Han [2,*]

1   Department of Safety Engineering, Dongguk University, Gyeongju Campus, Gyeongju 38066, Korea; parksungbum@dongguk.ac.kr or sbpark@dongguk.ac.kr
2   Department of Mechanical System Engineering, Dongguk University, Gyeongju Campus, Gyeongju 38066, Korea
*   Correspondence: skhan@dongguk.ac.kr; Tel.: +82-54-770-2222

Abstract: In this study, we examined the robust super-twisting sliding mode backstepping control (SBSC) method, which employed a tracking differentiator and nonlinear disturbance observer for a hexacopter unmanned aerial vehicle (UAV) system. To realize robust tracking control performance for a highly coupled nonlinear hexacopter UAV system, a super-twisting sliding mode control method was combined with designing stabilizing controls of backstepping control (BSC) applied to the UAV system. Furthermore, the differentiation issue of the virtual control and compensation of transformation error in the conventional BSC design were bypassed via a new continuous tracking differentiator structure. Additionally, a new disturbance observer based on the proposed tracking differentiator was considered to estimate uncertainties of the hexacopter UAV. Comparative simulation results demonstrated that the proposed tracking-differentiator-based SBSC scheme (PTSBSC) blended with the tracking differentiator and nonlinear disturbance observer exhibits improved performance when compared to that of conventional BSC and disturbance observer systems.

Keywords: hexacopter unmanned aerial vehicle; backstepping control; super-twisting sliding mode control; tracking differentiator; nonlinear disturbance observer

1. Introduction

Developments of the rechargeable battery source, brushless DC motor, and various related techniques lead to increased research unmanned aerial vehicles (UAVs). The multi-rotor UAVs exhibit significant advantages in terms of hovering capability and maneuverability involving side and backward movement, vertical take-off and landing in 3D space, and lower maintenance cost than other small aerial vehicles [1–4]. Thus, UAVs were initially used for military applications. However, recently, its applications were extended to agriculture, aerial photography, inspection, surveillance, rescue, transport monitoring, and exploration of inaccessible areas. Most multi-rotor UAVs adopted a four-rotor mounted quadrotor structure, and they exhibit limited power for heavy cargo delivery. Currently, UAVs mounted with more rotors, such as hexacopter and octocopter UAVs, when compared to four rotors, were developed to enforce lifting and higher capabilities in terms of flying time [5–10]. When considering the efficiency of UAVs, the hexacopter is more feasible than the octocopter because an increase in the number of rotors leads to an increase in size and cost.

However, safe and reliable flight of multi-rotor UAVs should be secured. This is because severe damages can result if the UAV falls or crashes, and the increased speed rotation of a multi-rotor can lead to more severe accidents. Thus, to guarantee safety and reliability in the flight of multi-rotor UAVs, an effective and robust controller is required to overcome the following challenges: (1) under-actuated control scheme for six degrees of

freedom (DOF) with four control inputs; (2) strongly coupled nonlinear dynamics between translational and rotational subsystems and kinematic coupling terms; and (3) uncertainties including external disturbances, such as wind and rain, in outdoor environment and unknown dynamics due to varying load.

Several control methods have been utilized to handle the above issues. Linear control schemes, including proportional-integral-derivative (PID) [7,9,11], linear quadratic regulator (LQR) [12,13], predictive control [14], and H_∞ control [15] have been initially applied for the fundamental flight task of the multi-rotor UAVs. However, these methods undergo their application limits due to performance degradation when the UAV leaves away its designed trimming points or accepts excessive perturbations. To handle these limits, recursive backstepping control (BSC) [6,16,17] is generally utilized as a baseline controller because BSC is appropriate for the aforementioned coupled higher order nonlinear systems and especially for multi-rotor UAVs [18–23]. The procedures for stabilizing system states are recursively repeated in the BSC design by utilizing virtual controllers, and the final controller is obtained in the last recursive step. Thus, a controller for any nonlinear system can be systematically designed without utilizing any linearization, which neglects useful nonlinearities.

Conversely, despite the popularity and advantage of the BSC scheme, there exist several disadvantages in the traditional BSC scheme. First, the virtual stabilizing controls contain the repeated differentiation terms with respect to virtual controls designed during the pre-recursive steps for high-order nonlinear systems. Hence, this leads to an increase in complexity. The tracking differentiator methods [24–30] were recently investigated as a potential solution. Furthermore, the second-order finite-time command filter [31–33] was considered to obtain improved properties to guarantee finite-time convergence and avoid increases in complexity, given that the traditional BSC schemes were designed in the point of infinite-time convergence. However, the traditional tracking differentiators exhibit the disadvantage of slow convergence time, though the recently developed tracking differentiators in [27–29] show more improved performance than those of the previous ones.

Second, most BSC systems were designed to be based on the nonlinear model dynamics in each recursive step and are then exposed to the uncertainty issue. Hence, they are sensitive to uncertainties, and control performances will be degraded when the parametric perturbations and external disturbances occur. Further efforts have been made to enforce robustness to uncertainty in the ordinary BSC system.

The first solution for the second issue is that BSC is typically combined with the first-order sliding mode control (SMC) [34] by utilizing the robustness property of SMC. However, there is a chattering disadvantage of the first order SMC [35–38].

As the second solution for the second issue, to enforce control performance by estimating and compensating uncertainties, several disturbance observers are developed [39–45]. A disturbance observer studied in [39,40] is applied to estimate uncertainties for nonlinear systems. However, it has the drawback that the observer is designed under the assumption of slow variation of uncertainties. An extended state observer (ESO) in [41,42] is developed on the position feedback, which is commonly obtained by integrating the velocity information of the system, especially for the multi-rotor UAVs. The long-time integration errors will influence the position information, which further degrade estimation accuracy of the observers. Disturbance observers utilizing a tracking differentiator to bypass the differentiation error in velocity feedback routine are developed in [43–45]. However, the convergence rate of the state of observer is slow, and the resulting estimation performance for uncertainties is degraded. Hence, to cope with the lower convergence performance in these observers, a more enhanced observer is required to achieve higher estimation and compensation of the uncertainties.

Motivated by the aforementioned works, as an alternative to the first-order SMC, the super-twisting algorithm (STA) [46–49] was developed because the STA offers the following advantages: it requires only the information on the sliding variable; it provides finite-time convergence to the origin for the sliding variable and its derivative; and it gener-

ates a continuous control signal to consequently adjust chattering. Furthermore, a novel continuous tracking differentiator based on the sine hyperbolic function is proposed to enhance lower performance traditional tracking differentiators. Finally, a novel disturbance observer based on the proposed tracking differentiator is examined to estimate the external disturbance in USVs. Therefore, in this study, a BSC system combined with STA (SBSC) is considered to realize finite-time convergence and robustness with respect to uncertainty over the conventional BSC system.

The contributions of this study are summarized as follows:

(1) The traditional BSC is combined with the STA to enforce insensitivity to variation of uncertainties of a hexacopter UAV system and bypass chattering in the traditional BSC combined with the first-order sliding mode control.

(2) The proposed SBSC control strategy for a hexacopter UAV improves finite settling-time convergence when compared to the traditional BSC system. Faster movements of a hexacopter UAV will be expected for a perturbed environmental situation.

(3) A novel continuous tracking differentiator based on the sine hyperbolic function is developed to obtain enhanced convergence of the state variable of the tracking differentiator. Thus, faster output of the command filter approximation on the derivative of the virtual control at each recursive step is acquired. The proposed tracking differentiator system exhibits improved performance when compared to the conventional system.

(4) An improved nonlinear disturbance observer can be designed by utilizing the proposed tracking differentiator. Hence, the performance of estimation and disturbance rejection for uncertainties of the hexacopter UAV control system are improved by utilizing the proposed disturbance observer.

Finally, the performance of the proposed control scheme is evaluated via sequential comparative simulation of a nonlinear hexacopter UAV system.

The rest of the paper is organized as follows. The nonlinear system model of UAV and tracking differentiator are presented in Section 2, and the design process for a SBSC is described in Section 3. Furthermore, stability analysis is discussed in Section 4, and simulation results for a hexacopter UAV system are provided in Section 5. Finally, the summary and conclusion of the study are presented in Section 6.

2. Preliminaries

2.1. UAV Dynamics and Problem Formulation

A hexacopter UAV has a mechanism for generating the required forces and torques. The nonlinear dynamics of a hexacopter, as presented in Figure 1 [10], is expressed as follows:

$$\dot{\boldsymbol{P}} = \boldsymbol{v}_b,$$
$$m\dot{\boldsymbol{v}}_b = \boldsymbol{R}_t \boldsymbol{F} - mg\boldsymbol{e}_z + \boldsymbol{F}_d, \tag{1}$$

$$\dot{\boldsymbol{\Theta}} = \boldsymbol{R}_r \boldsymbol{\omega}_b,$$
$$\boldsymbol{J}_b \dot{\boldsymbol{\omega}}_b = -\boldsymbol{\omega}_b \times \boldsymbol{J}_b \boldsymbol{\omega}_b + \boldsymbol{M}_b + \boldsymbol{M}_g + \boldsymbol{M}_d, \tag{2}$$

where $\boldsymbol{P} = [x, \, y, \, z]^T$ denotes position with respect to the inertia frame, $\boldsymbol{\Theta} = [\phi, \, \theta, \, \psi]^T$ denotes Euler angles, $\boldsymbol{v}_b = [u, v, w]^T$ and $\boldsymbol{\omega}_b = [p, \, q, \, r]^T$ denote linear and angular velocities, respectively, in the body-fixed frame. $\boldsymbol{J}_b = diag(J_x, J_y, J_z)$ denotes a symmetric positive definite moment of inertia matrix, $\boldsymbol{e}_z = [0 \ 0 \ 1]^T$; $\boldsymbol{M}_g$ denotes the resultant torque due to the gyroscopic effect, and $\boldsymbol{F}_d$ and $\boldsymbol{M}_d$ denote uncertainties, including parameter change, asymmetric structure, payload variation, rotor fluctuation, and aerodynamic drag, which are denoted as $\boldsymbol{F}_d = [d_x\dot{x}, \, d_y\dot{y}, \, d_z\dot{z}]^T$, $\boldsymbol{M}_g = \sum_{i=1}^{6} J_r(\boldsymbol{\omega}_b \times \boldsymbol{e}_z)\overline{\Omega}$, and $\boldsymbol{M}_d = [d_\phi\dot{\phi}, \, d_\theta\dot{\theta}, d_\psi\dot{\psi}]^T$. J_r denotes the moment of inertia of each rotor and $\overline{\Omega} = \Omega_1 - \Omega_2 + \Omega_3 - \Omega_4 \, \Omega_5 + \Omega_6$, and Ω_i denotes the speed of rotor i. The translation force $\boldsymbol{F}_d$ contains gravity, main thrust force,

and other force components. The airframe orientation in space is provided using a rotation matrix $\boldsymbol{R}_t$ from the body frame to the navigation frame, and $\boldsymbol{\omega}_b$ is expressed as follows:

$$\boldsymbol{R}_t = \begin{bmatrix} c\theta c\psi & s\phi s\theta c\psi - c\phi s\psi & c\phi s\theta c\psi + s\phi s\psi \\ c\theta s\psi & s\phi s\theta s\psi + c\phi c\psi & c\phi s\theta s\psi - s\phi c\psi \\ -s\theta & s\phi c\theta & c\phi c\theta \end{bmatrix}, \tag{3}$$

$$\boldsymbol{\omega}_b = \boldsymbol{R}_r = \begin{bmatrix} 1 & 0 & -s\theta \\ 0 & c\phi & c\theta s\phi \\ 0 & -s\phi & c\theta c\phi \end{bmatrix} \begin{bmatrix} \dot{\phi} \\ \dot{\theta} \\ \dot{\psi} \end{bmatrix}, \tag{4}$$

where $s(\cdot)$ and $c(\cdot)$ denote $\sin(\cdot)$ and $\cos(\cdot)$, respectively. The lift force $\boldsymbol{F} = [0, 0, u_f]^T$ and torque $\boldsymbol{M}_b = [u_\phi, u_\theta, u_\psi]^T$ are generated by rotors with respect to body-fixed frame as follows:

$$\begin{aligned} u_f &= \sum_{i=1}^{6} F_i, \\ u_\phi &= -\tfrac{1}{2}F_1 l + \tfrac{1}{2}F_2 l + F_3 l + \tfrac{1}{2}F_4 l - \tfrac{1}{2}F_5 l - F_6 l, \\ u_\theta &= -\tfrac{\sqrt{3}}{2}F_1 l - \tfrac{\sqrt{3}}{2}F_2 l + \tfrac{\sqrt{3}}{2}F_4 l + \tfrac{\sqrt{3}}{2}F_5 l, \\ u_\psi &= C_d(-\Omega_1^2 + \Omega_2^2 - \Omega_3^2 + \Omega_4^2 - \Omega_5^2 + \Omega_6^2), \end{aligned} \tag{5}$$

where $F_i = C_p \Omega_i^2$ denotes the force generated in the i-th rotor, $C_d > 0$ and $C_p > 0$ denote coefficients of drag and thrust of the propeller, respectively, and l denotes the distance from rotors to the center of mass. Given the perturbation of the mass of the body due to the loading of the carrying object, (1) is expressed as follows:

$$m_0 \dot{\boldsymbol{v}}_b = \boldsymbol{R}_t \boldsymbol{F} - m_0 g \boldsymbol{e}_z + \boldsymbol{U}_b, \tag{6}$$

where $\boldsymbol{U}_b = -\Delta m \dot{\boldsymbol{v}}_b + \boldsymbol{F}_d$ and Δm denotes a mass perturbation. Based on the above results, the translational dynamics equations of the hexacopter can be expressed as follows:

$$\ddot{x} = \frac{1}{m_0}(c\phi s\theta c\psi + s\phi s\psi)u_f - \rho_x, \tag{7}$$

$$\ddot{y} = \frac{1}{m_0}(c\phi s\theta \sin\psi - s\phi c\psi)u_f - \rho_y, \tag{8}$$

$$\ddot{z} = -g + \frac{1}{m_0}(c\phi c\theta)u_f - \rho_z, \tag{9}$$

where $\rho_x = \frac{1}{m_0}(\Delta m \ddot{x} - d_x \dot{x})$, $\rho_y = \frac{1}{m_0}(\Delta m \ddot{y} - d_y \dot{y})$, and $\rho_z = \frac{1}{m_0}(\Delta m \ddot{z} - d_z \dot{z})$. Next, the rotational dynamic equations are expressed as follows:

$$\ddot{\phi} = \dot{\theta}\dot{\psi}\frac{J_y - J_z}{J_x} - \frac{J_r}{J_x}\dot{\theta}\overline{\Omega} + \frac{l}{J_x}u_\phi - \rho_\phi, \tag{10}$$

$$\ddot{\theta} = \dot{\psi}\dot{\phi}\frac{J_z - J_x}{J_y} + \frac{J_r}{J_y}\dot{\phi}\overline{\Omega} + \frac{l}{J_y}u_\theta - \rho_\theta, \tag{11}$$

$$\ddot{\psi} = \dot{\phi}\dot{\theta}\frac{J_x - J_y}{J_z} + \frac{l}{J_z}u_\psi - \rho_\psi, \tag{12}$$

where $\rho_\phi = \frac{d_\phi l}{J_x}\dot{\phi}$, $\rho_\theta = \frac{d_\theta l}{J_y}\dot{\theta}$, and $\rho_\psi = \frac{d_\psi l}{J_z}\dot{\psi}$.
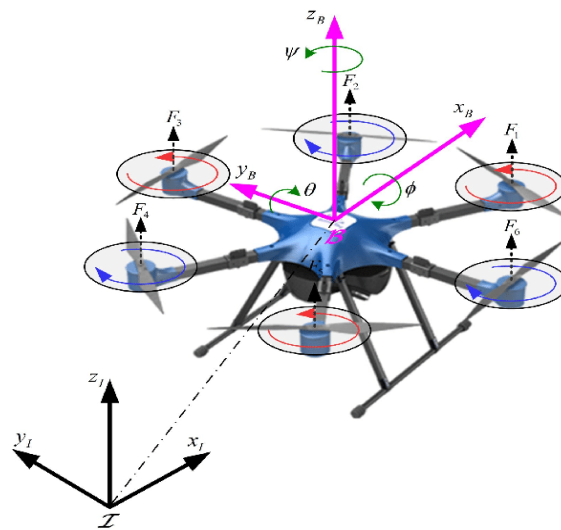
Figure 1. Description of the hexacopter UAV.

2.2. Tracking Differentiator

In this section, a tracking differentiator is considered to avoid the differentiation of the virtual controls in the BSC scheme.

Theorem 1 ([26])**.** *If any solution of the following system:*

$$\begin{aligned} \dot{z}_1 &= z_2, \\ \dot{z}_2 &= f(z_1, z_2) \end{aligned} \tag{13}$$

satisfies $z_1 \to 0$, $z_2 \to 0$ *as* $t \to \infty$*, then for an arbitrary bounded and integrable input function* α *and a constant* $T > 0$*, the solution of the following system*

$$\begin{aligned} \dot{\chi}_1 &= \chi_2, \\ \dot{\chi}_2 &= R^2 f(\chi_1 - \alpha, \chi_2/R) \end{aligned} \tag{14}$$

satisfies $\lim_{R \to \infty} \int_0^T |\chi_1 - \alpha| dt = 0$ *if the solutions of (14) satisfy* $\chi_1 \to 0$ *and* $\chi_2 \to 0$ *as* $t \to \infty$*.*

Theorem 2 ([26])**.** *Consider the following system*

$$\begin{aligned} \dot{\chi}_1 &= \chi_2, \\ \dot{\chi}_2 &= -r_1 \sinh(a_1 \chi_1) - r_2 \sinh(a_2 \chi_2). \end{aligned} \tag{15}$$

The system (15) is global uniformly asymptotically stable if $r_i > 0$ *and* $a_i > 0$, $i = 1, 2$, *are satisfied.*

Theorem 3. *Consider the following system*

$$\begin{aligned} \dot{\chi}_1 &= \dot{\chi}_2, \\ \dot{\chi}_2 &= -R^2 [r_1 \sinh(a_1 \varphi_1(\chi_1 - \alpha)) + r_2 \sinh(a_2 \varphi_2(\chi_2)/R)], \end{aligned} \tag{16}$$

where $\varphi_1(\chi_1 - \alpha) = \kappa sig^{1/2}(\chi_1 - \alpha) + (1 - \kappa)sig^{(2+\gamma)/2}(\chi_1 - \alpha)$, $\varphi_2(\chi_2) = sig^{1/2}(\chi_2)$, $sig^{1/2}(\cdot) = |\cdot|^{1/2} sign(\cdot)$, $0 < \kappa < 1$ *and* $0 < \gamma < 1$ *are constants. For an arbitrary bounded and integrable function* α *and a constant* $T > 0$, $\lim_{R \to \infty} \int_0^T |\chi_1 - \alpha| dt = 0$ *can be obtained if the positive conditions of all parameters are satisfied.*

Proof. Transforming $\omega_1 = \chi_1 - \alpha$ and $\omega_2 = \chi_2/R$ in (16), it follows that $\omega_1 r_1 \sinh(a_1 \varphi(\omega_1)) \geq 0$ because $\sinh(\cdot)$ is an odd function. Then, $\int_0^{\omega_1} r_1 \sinh(a_1 \varphi(\tau)) d\tau \geq 0$, where τ means an introduced integral variable. Thus, we can consider the following Lyapunov function:

$$V(\omega_1, \omega_2) = R^2 \int_0^{z_1} r_1 \sinh(a_1 \varphi(\tau)) d\tau + \frac{1}{2}\omega_2^2. \tag{17}$$

Taking the time derivative of (17) and using (16) result in

$$\begin{aligned}
\dot{V}(\omega_1, \omega_2) &= R_2^2 r_1 \sinh(a_1 \varphi(\omega_1))\omega_2 + \omega_2 \dot{\omega}_2 \\
&= R_2^2 r_1 \sinh(a_1 \varphi(\omega_1))\omega_2 - R^2 \omega_2 [r_1 \sinh(a_1 \varphi_1(\omega_1)) + r_2 \sinh(a_2 \varphi_2(\omega_2))] \\
&= -R^2 \omega_2 r_2 \sinh(a_2 \varphi_2(\omega_2)) \leq 0
\end{aligned} \tag{18}$$

Thus, it is sure that $\dot{V}(\omega_1, \omega_2) = 0$ only when $\omega_2 = 0$. Based on (16), when $\omega_2 = 0$, ω_1 will always be equivalent to zero. If $\omega_1 \to \infty$ and $\omega_2 \to \infty$, we obtain that $V(\omega_1, \omega_2) \to \infty$. Hence, the solutions of $\dot{V}(\omega_1, \omega_2)$ do not include any other whole trajectory, except the origin (0,0).

Therefore, the system (16) is globally asymptotically stable. This concludes the proof. $\square$

For comparison of the above differentiators, three tracking differentiators were selected. The first one, which is proposed by Yang et al. [27], is the following hyperbolic tangent tracking differentiator:

$$\begin{aligned}
\dot{\chi}_1 &= \chi_2 \\
\dot{\chi}_2 &= -R^2 [r_1 tansig(a_1(\chi_1 - \alpha)) + r_2 tansig(a_1 \chi_2/R)],
\end{aligned} \tag{19}$$

where $tansig(a_1 x) = \frac{2}{e^{-2a_1 x}+1} - 1$. The second one, which was proposed by Zong et al. [28,29], is the tangent sigmoid function tracking differentiator given by

$$\begin{aligned}
\dot{\chi}_1 &= \chi_2 \\
\dot{\chi}_2 &= -R^2 [r_1\{(\chi_1 - \alpha) + |\chi_1 - \alpha|^\beta tansig(a_1(\chi_1 - \alpha))\} + r_2\{\chi_2/R + |\chi_2/R|^\beta tansig(a_2 \chi_2/R)\}],
\end{aligned} \tag{20}$$

where $0 < \beta < 1$ is a constant. The third one, the first-order sliding mode tracking differentiator proposed by Levant [30,31], is considered, which is described as

$$\begin{aligned}
\dot{\chi}_1 &= v_1 = -r_1 |\chi_1 - \alpha|^{1/2} sign(\chi_1 - \alpha) + \chi_2, \\
\dot{\chi}_2 &= -r_2 sign(\chi_2 - v_1),
\end{aligned} \tag{21}$$

3. Design of Controller and Nonlinear Disturbance Observer

3.1. Design of Altitude Controller

The vertical displacement is determined by the altitude controller. The state equation for altitude dynamics in (8) can be expressed as follows:

$$\begin{aligned}
\dot{x}_1 &= x_2, \\
\dot{x}_2 &= \frac{1}{m}(\cos\phi \cos\theta)u_1 - g - \rho_2,
\end{aligned} \tag{22}$$

where the altitude state variable $x_1 = z$, $x_2 = \dot{z}$, and $u_1 = u_z$. By introducing the command trajectory x_{1d} in the z-coordinate, the sliding mode surfaces to include the tracking error and new states are defined as follows:

$$s_1 = x_1 - x_{1d} - \xi_{11}, \tag{23}$$

$$s_2 = x_2 - \chi_{11} - \xi_{12}, \tag{24}$$

where the sliding mode surfaces include the tracking error and the compensating signals. The state variables ξ_{11} and ξ_{12} in (23) and (24) are obtained from the dynamics of the compensating signals expressed as follows:

$$\dot{\xi}_{11} = -k_{11}\xi_{11} + \xi_{12} + \chi_{11} - \alpha_1 - \beta_{\zeta,11}sig^{1/2}(\xi_{11}),$$
$$\dot{\xi}_{12} = -k_{12}\xi_{12} - \xi_{11} - \beta_{\zeta,12}sig^{1/2}(\xi_{12}), \tag{25}$$

where $\beta_{\zeta,ij} > 0$, $i = 1, 2$, $j = 1, 2$, denote constants. Next, the output of the tracking differentiator χ_{11} is obtained from the tracking differentiator dynamics described in Theorem (3):

$$\dot{\chi}_{11} = \chi_{12},$$
$$\dot{\chi}_{12} = -R_1^2[r_{11}\sinh(a_{11}\varphi_{11}(\chi_{11}, \alpha_1)) + r_{12}\sinh(a_{12}R_1^{-1}\varphi_{12}(\chi_{12}))], \tag{26}$$

where $\varphi_{11}(\chi_{11}, \alpha_1) = \kappa_1 sig^{1/2}(\chi_{11} - \alpha_1) + (1 - \kappa_1)sig^{(2+\gamma_1)/2}(\chi_{11} - \alpha_1)$, $\varphi_{12}(\chi_{12}) = sig^{1/2}(\chi_{12})$, $sig^{1/2}(\cdot) = |s_i|^{1/2}sign(\cdot)$. α_1 denotes the virtual control defined later, $r_{1i} > 0$ and $a_{1i} > 0$ are constants, and $\kappa_1 > 1$ and $0 < \gamma_1 < 1$ denote constants. We define the following super-twisting state variable vectors to design the controller using the variables defined previously.

$$\zeta_1 = \begin{bmatrix} \zeta_{11} & \zeta_{12} \end{bmatrix}^T$$
$$= \begin{bmatrix} k_{11}s_1 + sig^{1/2}(s_1) \\ -k_{12}\int_0^t [k_{11}^2 s_1 + \frac{3k_{11}}{2}sig^{1/2}(s_1) + \frac{1}{2}sign(s_1)]d\tau \end{bmatrix}, \tag{27}$$

$$\zeta_2 = \begin{bmatrix} \zeta_{21} & \zeta_{22} \end{bmatrix}^T$$
$$= \begin{bmatrix} k_{21}s_2 + sig^{1/2}(s_2) \\ -k_{22}\int_0^t [k_2^2 s_2 + \frac{3k_2}{2}sig^{1/2}(s_2) + \frac{1}{2}sign(s_2)]d\tau \end{bmatrix}. \tag{28}$$

The super-twisting state variable vectors consist of the sliding mode surfaces and signum functions. Using the definition in (23), the time derivative of the components of the state vectors in (27) and (28) can then be written as

$$\dot{\zeta}_{11} = k_{11}\dot{s}_1 + \frac{1}{2}|s_1|^{-1/2}\dot{s}_1$$
$$= \mu_1(x_2 - \dot{x}_{1d} - \dot{\xi}_1)$$
$$= \mu_1(x_2 - \dot{x}_{1d} + k_{11}\xi_{11} - \xi_{12} - \chi_{11} + \alpha_1 + \beta_{\xi,11}sig^{1/2}(\xi_{11})) \tag{29}$$
$$= \mu_1(s_2 - \dot{x}_{1d} + k_{11}\xi_{11} + \alpha_1 + \beta_{\xi,11}sig^{1/2}(\xi_{11})),$$

$$\dot{\zeta}_{12} = -\mu_1 k_{12}\zeta_{11}, \tag{30}$$

$$\dot{\zeta}_{21} = k_{21}\dot{s}_2 + \frac{1}{2}|s_2|^{-1/2}\dot{s}_2$$
$$= \mu_2\left(\frac{1}{m}(\cos\phi\cos\theta)u_1 - g - \rho_2 - \chi_{12} + k_{12}\xi_{12} + \xi_{11} + \beta_{\xi,12}sig^{1/2}(\xi_{12})\right), \tag{31}$$

$$\dot{\zeta}_{22} = -\mu_2 k_{22}\zeta_{21}, \tag{32}$$

where $\mu_1 = k_{11} + \frac{1}{2}|s_1|^{-1/2}$ and $\mu_2 = k_{21} + \frac{1}{2}|s_2|^{-1/2}$. We can select the virtual control from (29) and control input from (31) as follows:

$$\alpha_1 = -k_{11}\zeta_{11} - k_{11}\xi_{11} - \beta_{\xi,11}sig^{1/2}(\xi_{11}) + \dot{x}_{1d} + \zeta_{12}, \tag{33}$$

$$u_1 = \frac{m}{\cos\phi\cos\theta}(-k_{21}\zeta_{21} - k_{21}\xi_{12} + g + \hat{\rho}_2 + \chi_{12} - \xi_{11} - \beta_{\xi,12}sig^{1/2}(\xi_{12})$$
$$- \frac{\xi_1\eta_1}{\xi_2\eta_2}s_2 + \zeta_{22}), \tag{34}$$

where $\eta_k = (c_k + 4\varepsilon_k^2)\zeta_{k1} - 2\varepsilon_k\zeta_{k2}$, $c_k > 0$ and $\varepsilon_k > 0$, $k = 1, 2$, are constants, the virtual control input α_1 denotes the recursive input, and u_1 denotes the final control input. Using (33) and (34), (29) and (31) can be expressed as follows:

$$\dot{\zeta}_{11} = -k_{11}\mu_1\zeta_{11} + \mu_1\zeta_{12} + \mu_1 s_2, \tag{35}$$

$$\dot{\zeta}_{21} = -\mu_2 k_{21}\zeta_{21} + \mu_2\zeta_{22} - \frac{\mu_1\eta_1}{\eta_2}s_2 - \mu_2\tilde{\rho}_2, \tag{36}$$

where $\tilde{\rho}_2 = \rho_2 - \hat{\rho}_2$ denotes the estimate error. Considering the above results, the following compact expressions can be obtained:

$$\dot{\zeta}_1 = -\mu_1 \begin{bmatrix} k_{11} & -1 \\ k_{12} & 0 \end{bmatrix} \begin{bmatrix} \zeta_{11} \\ \zeta_{12} \end{bmatrix} + \begin{bmatrix} \mu_1 s_2 \\ 0 \end{bmatrix}, \tag{37}$$

$$\dot{\zeta}_2 = -\mu_2 \begin{bmatrix} k_{21} & -1 \\ k_{22} & 0 \end{bmatrix} \begin{bmatrix} \zeta_{21} \\ \zeta_{22} \end{bmatrix} + \begin{bmatrix} -\frac{\mu_1\eta_1}{\eta_2}s_2 \\ 0 \end{bmatrix} + \begin{bmatrix} \mu_2\tilde{\rho}_2 \\ 0 \end{bmatrix}. \tag{38}$$

We define the Lyapunov function candidate as follows:

$$V_1 = \frac{1}{2}\zeta_1^T P_1 \zeta_1 + \frac{1}{2}\zeta_2^T P_2 \zeta_2, \tag{39}$$

where P_k denotes positive definite matrices defined as follows:

$$P_k = \begin{bmatrix} c_k + 4\varepsilon_k^2 & -2\varepsilon_k \\ -2\varepsilon_k & 1 \end{bmatrix}, \; k = 1, 2.$$

Differentiating (39) with respect to time and using (37) and (38) result in the following expression:

$$\begin{aligned}
\dot{V}_1 &= \zeta_1^T P_1 \dot{\zeta}_1 + \zeta_2^T P_2 \dot{\zeta}_2 \\
&\leq -\mu_1\zeta_1^T Q_1 \zeta_1 + \mu_1\eta_1 s_2 - \mu_2\zeta_2^T Q_2\zeta_2 + \tilde{\rho}_2\mu_2\eta_2 - \mu_1\eta_1 s_2 \\
&\leq -\sum_{k=1}^{2}\mu_k\zeta_k^T Q_k\zeta_k + \delta_2,
\end{aligned} \tag{40}$$

where $\eta_k = (c_k + 4\varepsilon_k^2)\zeta_{k1} - 2\varepsilon_k\zeta_{k2}$, $|\tilde{\rho}_2\mu_2\eta_2| \leq \delta_2$, and the positive definite matrix

$$Q_k = \begin{bmatrix} 2k_{k1}(c_k + 4\varepsilon_k^2) - 4k_{k2}\varepsilon_k & (c_k + 4\varepsilon_k^2) - 2\varepsilon_k k_{k1} + k_{k2} \\ c_k + 4\varepsilon_k^2 - 2\varepsilon_k k_{k1} + k_{k2} & 4\varepsilon_k \end{bmatrix}, k = 1, 2.$$

3.2. Design of Longitudinal and Latitudinal Controllers

Let us define the state variables for x-, y-axes and roll, pitch axes from (6), (7), (9), and (10) as $x_3 = [x \; y]^T$, $x_4 = [\dot{x} \; \dot{y}]^T$, $x_5 = [\phi \; \theta]^T$, and $x_6 = [\dot{\phi} \; \dot{\theta}]^T$. The state–space model is represented as follows:

$$\dot{x}_3 = x_4, \dot{x}_4 = R_4(\psi, u_1)T_4(x_5) - \rho_4, \tag{41}$$

$$\dot{x}_5 = x_6, \dot{x}_6 = f_6 + g_6 u_{\phi\theta} - \rho_6, \tag{42}$$

where $R_4(\psi, u_1) = \frac{1}{m}\begin{bmatrix} \cos\psi & \sin\psi \\ \sin\psi & -\cos\psi \end{bmatrix}u_1$, $T_4(x_5) = [\cos\phi\sin\theta \; \sin\phi]^T$, $\rho_4 = [\rho_x \; \rho_y]^T$, $g_6 = diag(l/J_x \; l/J_y)$, $u_{\phi\theta} = [\tau_\phi \; \tau_\theta]^T$, and $f_6 = [\dot{\theta}\dot{\psi}(J_y - J_z)/J_x + J_r\dot{\theta}\Omega_r/J_x \; \dot{\psi}\dot{\phi}(J_z - J_x)/J_y - J_r\dot{\phi}\Omega_r/J_y]^T$, $\rho_6 = [\rho_\phi \; \rho_\theta]^T$. We define the sliding mode vectors including the tracking command, errors, and state variables as

$$s_3 = x_3 - x_{3d} - \zeta_{31}, \tag{43}$$

$$s_4 = x_4 - \chi_{31} - \xi_{32}, \tag{44}$$

$$s_5 = x_5 - x_{5d} - \xi_{51}, \tag{45}$$

$$s_6 = x_6 - \chi_{51} - \xi_{52}. \tag{46}$$

In the sliding mode surfaces, the dynamics of the compensating signals ξ_{3j}, $j = 1, 2$, is described as

$$\begin{aligned}
\dot{\xi}_{i1} &= -k_{i1}\xi_{i1} + \xi_{12} + \chi_{i1} - \alpha_i - \beta_{\zeta,i1}sig^{1/2}(\xi_{i1}), \\
\dot{\xi}_{i2} &= -k_{i2}\xi_{i2} - \xi_{i1} - \beta_{\zeta,i2}sig^{1/2}(\xi_{i2}), i = 3, 5,
\end{aligned} \tag{47}$$

where $\beta_{\zeta,ij} > 0$, $i = 3, 5$, $j = 1, 2$, are constants. Furthermore, χ_{i1} is obtained from the tracking differentiator described as follows:

$$\begin{aligned}
\dot{\chi}_{i1} &= \chi_{i2}, \\
\dot{\chi}_{i2} &= -R_i^2[r_{i1}\sinh(a_{i1}\varphi_{i1}(\chi_{i1}, \alpha_i)) + r_{i2}\sinh(a_{i2}R_i^{-1}\varphi_{i2}(\chi_{i2}))], i = 3, 5,
\end{aligned} \tag{48}$$

where $\varphi_{i1}(\chi_{i1}, \alpha_i) = \kappa_i sig^{1/2}(\chi_{i1} - \alpha_i) + (1 - \kappa_i)sig^{(2+\gamma_i)/2}(\chi_{i1} - \alpha_i)$, $\varphi_{i2}(\chi_{i2}) = sig^{1/2}(\chi_{i2})$, $\kappa_i > 1$ and $0 < \gamma_i < 1$ are constants. We define the following super-twisting state variable vectors to design the controller using the variables defined previously

$$\zeta_3 = \begin{bmatrix} \zeta_{31} & \zeta_{32} \end{bmatrix}^T = \begin{bmatrix} k_{31}s_3 + sig^{1/2}(s_3) \\ -k_{32}\int_0^t [k_{31}^2 s_3 + \frac{3k_{32}}{2}sig^{1/2}(s_3) + \frac{1}{2}sign(s_3)]d\tau \end{bmatrix}, \tag{49}$$

$$\zeta_4 = \begin{bmatrix} \zeta_{41} & \zeta_{42} \end{bmatrix}^T = \begin{bmatrix} k_{41}s_4 + sig^{1/2}(s_4) \\ -k_{42}\int_0^t [k_{41}^2 s_4 + \frac{3k_{42}}{2}sig^{1/2}(s_4) + \frac{1}{2}sign(s_4)]d\tau \end{bmatrix}, \tag{50}$$

$$\zeta_5 = \begin{bmatrix} \zeta_{51} & \zeta_{52} \end{bmatrix}^T = \begin{bmatrix} k_{51}s_5 + sig^{1/2}(s_5) \\ -k_{52}\int_0^t [k_{51}^2 s_5 + \frac{3k_{51}}{2}sig^{1/2}(s_5) + \frac{1}{2}sig^{1/2}(s_5)]d\tau \end{bmatrix}, \tag{51}$$

$$\zeta_6 = \begin{bmatrix} \zeta_{61} & \zeta_{62} \end{bmatrix}^T = \begin{bmatrix} k_{61}s_6 + sig^{1/2}(s_6) \\ -k_{62}\int_0^t [k_{61}^2 s_6 + \frac{3k_{61}}{2}sig^{1/2}(s_6) + \frac{1}{2}sig^{1/2}(s_6)]d\tau \end{bmatrix}. \tag{52}$$

The differentiation of the above state vectors is as follows:

$$\dot{\zeta}_3 = \begin{bmatrix} \dot{\zeta}_{31} & \dot{\zeta}_{32} \end{bmatrix}^T = \begin{bmatrix} \mu_3(s_4 + \varsigma_{31} + \xi_{41} - \dot{x}_{3d} - \dot{\xi}_{31}) \\ -\mu_3 k_{31}\zeta_{31} \end{bmatrix}, \tag{53}$$

$$\dot{\zeta}_4 = \begin{bmatrix} \dot{\zeta}_{41} & \dot{\zeta}_{42} \end{bmatrix}^T = \begin{bmatrix} \mu_4(R_4(\psi, u_1)T_4(x_5) - \rho_4 - \dot{\chi}_{31} - \dot{\xi}_{32}) \\ -\mu_4 k_{41}\zeta_{41} \end{bmatrix}, \tag{54}$$

$$\dot{\zeta}_5 = \begin{bmatrix} \dot{\zeta}_{51} & \dot{\zeta}_{52} \end{bmatrix}^T = \begin{bmatrix} \mu_5(s_6 + \chi_{51} + \xi_6 - \dot{x}_{5d} - \dot{\xi}_{51}) \\ -\mu_5 k_{51}\zeta_{51} \end{bmatrix}, \tag{55}$$

$$\dot{\zeta}_6 = \begin{bmatrix} \dot{\zeta}_{61} & \dot{\zeta}_{62} \end{bmatrix}^T = \begin{bmatrix} \mu_6(f_6 + g_6 u_{\phi\theta} - \rho_6 - \dot{\chi}_{51} - \dot{\xi}_{52}) \\ -\mu_6 k_{61}\zeta_{61} \end{bmatrix}, \tag{56}$$

where $\mu_i = k_{ij} + \frac{1}{2}|s_i|^{-1/2}$, $i = 3, 4, 5, 6$, $j = 1, 2$. We can select the virtual controls α_i, $i = 3, 5$ for the recursive input, and control inputs u_i, $i = 2, 3$ as follows:

$$\alpha_3 = -k_{31}\zeta_{31} - k_{31}\xi_{31} - \beta_{\xi,31}sig^{1/2}(\xi_{31}) + \dot{x}_{3d} + \zeta_{32}, \tag{57}$$

$$\alpha_5 = -k_{51}\zeta_{51} - k_{51}\xi_{51} - \beta_{\xi,51}sig^{1/2}(\xi_{51}) + \dot{x}_{5d} + \zeta_{52}, \tag{58}$$

$$\begin{aligned}
u_2 = T_4(x_5) = R_4^{-1}(\psi, u_1)(&-k_{41}\zeta_{41} - k_{41}\xi_{42} + \hat{\rho}_4 + \chi_{32} - \xi_{41} \\
&-\beta_{\xi,41}sig^{1/2}(\xi_{41}) - \xi_4^{-1}\eta_4^{-1}\xi_3\eta_3 s_4 + \zeta_{42}),
\end{aligned} \tag{59}$$

$$u_3 = u_{\phi\theta} = g_6^{-1}(-k_{61}\zeta_{61} - k_{61}\xi_{61} - f_6 + \hat{\rho}_6 + \chi_{52} - \xi_{61} \\ -\beta_{\xi,61}sig^{1/2}(\xi_{61}) - \xi_6^{-1}\eta_6^{-1}\xi_5\eta_5 s_6 + \zeta_{62}) \tag{60}$$

where $R_4^{-1} = \begin{bmatrix} \cos\psi & \sin\psi \\ \sin\psi & -\cos\psi \end{bmatrix}^{-1} = \begin{bmatrix} \cos\psi & \sin\psi \\ \sin\psi & -\cos\psi \end{bmatrix}$, $\eta_k = (c_k + 4\varepsilon_k^2)\zeta_{k1} - 2\varepsilon_k\zeta_{k2}$, $c_k > 0$ and $\varepsilon_k > 0, k = 3, 4, 5, 6$, are constants. Next, substituting these controls into the dynamics of the compensating signals given in (47) and repeating the procedures of the previous step, we obtain the following compact expressions for the super-twisting state vector:

$$\dot{\zeta}_j = -\mu_j \begin{bmatrix} k_{j1} & -1 \\ k_{j2} & 0 \end{bmatrix} \begin{bmatrix} \zeta_{j1} \\ \zeta_{j2} \end{bmatrix} + \begin{bmatrix} \mu_j s_j \\ 0 \end{bmatrix}, j = 3, 5, \tag{61}$$

$$\dot{\zeta}_k = -\mu_k \begin{bmatrix} k_{k1} & -1 \\ k_{k2} & 0 \end{bmatrix} \begin{bmatrix} \zeta_{k1} \\ \zeta_{k2} \end{bmatrix} + \mu_k \begin{bmatrix} \widetilde{\rho}_k \\ 0 \end{bmatrix} + \begin{bmatrix} -\eta_k^{-1}\mu_{k-1}\eta_{k-1}s_k \\ 0 \end{bmatrix}, k = 4, 6, \tag{62}$$

where $\widetilde{\rho}_k = \rho_k - \hat{\rho}_k, k = 4, 6$. The Lyapunov function candidate with (60) and (61) is defined as follows:

$$V_2 = \sum_{k=3}^{6} \frac{1}{2}\zeta_k^T P_k \zeta_k, \tag{63}$$

where P_k denotes positive definite matrices defined as follows:

$$P_k = \begin{bmatrix} c_k + 4\varepsilon_k^2 & -2\varepsilon_k \\ -2\varepsilon_k & 1 \end{bmatrix}, k = 3, 4, 5, 6.$$

The time derivative of (63) leads to the following expression:

$$\dot{V}_2 \leq -\mu_3\zeta_3^T Q_3 \zeta_3 - \mu_5\zeta_5^T Q_5\zeta_5 + \mu_3\eta_3 s_3 + \mu_5\eta_5 s_5 - \mu_4\zeta_4^T Q_4\zeta_4 - \mu_6\zeta_6^T Q_6\zeta_6 - \mu_3\eta_3 s_3 \\ -\mu_5\eta_5 s_5 + \widetilde{\rho}_4^T \mu_4\eta_4 + \widetilde{\rho}_6^T\mu_6\eta_6 \\ \leq -\sum_{k=3}^{6}\mu_k\zeta_k^T Q_k\zeta_k + \delta_4 + \delta_6, \tag{64}$$

where $|\widetilde{\rho}_4^T\mu_4\eta_4| \leq \delta_4$, $|\widetilde{\rho}_6^T\mu_6\eta_6| \leq \delta_6$, and the positive definite matrix

$$Q_k = \begin{bmatrix} 2k_{k1}(c_k + 4\varepsilon_k^2) - 4k_{k2}\varepsilon_k & (c_k + 4\varepsilon_k^2) - 2\varepsilon_k k_{k1} + k_{k2} \\ c_k + 4\varepsilon_k^2 - 2\varepsilon_k k_{k1} + k_{k2} & 4\varepsilon_k \end{bmatrix}, k = 3, 4, 5, 6.$$

3.3. Design of the Heading Controller

Let us define the state variable for the yaw axis from (11) as $x_7 = \psi$ and $x_8 = \dot{\psi}$. Hence, the state–space model can be represented as follows:

$$\dot{x}_7 = x_8, \dot{x}_8 = \dot{\phi}\dot{\theta}\frac{J_x - J_y}{J_z} + \frac{l}{J_z}\tau_\psi - \rho_\psi = f_8 + g_8 u_4 - \rho_8, \tag{65}$$

where $f_8 = \dot{\phi}\dot{\theta}\frac{J_x - J_y}{J_z}$, $g_8 = \frac{l}{J_z}$, and $\rho_8 = \rho_\psi$. The tracking error and new states are defined as follows:

$$s_7 = x_7 - x_{7d} - \xi_{71}, \tag{66}$$

$$s_8 = x_8 - \chi_{71} - \xi_{72}. \tag{67}$$

The compensating signals included in (66) and (67) are obtained from the following dynamics:

$$\dot{\xi}_{71} = -k_{71}\xi_{71} + \xi_{72} + \chi_{71} - \alpha_7 - \beta_{\zeta,71}sig^{1/2}(\xi_{71}), \\ \dot{\xi}_{72} = -k_{72}\xi_{72} - \xi_{71} - \beta_{\zeta,72}sig^{1/2}(\xi_{72}). \tag{68}$$

where $\beta_{\zeta,7j} > 0$, $j = 1, 2$ are constants. In (67), χ_{71} denotes the output of the tracking differentiator expressed as follows:

$$
\begin{aligned}
\dot{\chi}_{71} &= \chi_{72}, \\
\dot{\chi}_{72} &= -R_7^2[r_{71}\sinh(a_{71}\varphi_{71}(\chi_{71}, \alpha_7)) + r_{72}\sinh(a_{72}R_7^{-1}\varphi_{72}(\chi_{72}))],
\end{aligned}
\tag{69}
$$

where $\varphi_{717}(\varsigma_{71}, \alpha_7) = \kappa_7 sig^{1/2}(\chi_{71} - \alpha_7) + (1 - \kappa_7)sig^{(2+\gamma_7)/2}(\chi_{71} - \alpha_7)$, $\varphi_{72}(\chi_{72}) = sig^{1/2}(\chi_{72})$, $\kappa_7 > 1$ and $0 < \gamma_7 < 1$ are constants. The super-twisting state variable vectors are defined as

$$
\zeta_7 = [\zeta_{71} \; \zeta_{72}]^T = \begin{bmatrix} k_7 s_7 + sig^{1/2}(s_7) \\ -k_{72}\int_0^t [k_7^2 s_7 + \frac{3k_7}{2}sig^{1/2}(s_7) + \frac{1}{2}sign(s_7)]d\tau \end{bmatrix},
\tag{70}
$$

$$
\zeta_8 = [\zeta_{81} \; \zeta_{82}]^T, = \begin{bmatrix} k_8 s_8 + sig^{1/2}(s_8) \\ -k_{82}\int_0^t [k_8^2 s_8 + \frac{3k_8}{2}sig^{1/2}(s_8) + \frac{1}{2}sign(s_8)]d\tau \end{bmatrix},
\tag{71}
$$

Next, the time derivatives of the state vector to design the controllers are given by

$$
\dot{\zeta}_7 = [\dot{\zeta}_{71} \; \dot{\zeta}_{72}]^T = \begin{bmatrix} \mu_7(x_8 - \dot{x}_{7d} - \dot{\xi}_{71}) \\ -\mu_7 k_{72}\zeta_{71} \end{bmatrix},
\tag{72}
$$

$$
\dot{\zeta}_8 = [\dot{\zeta}_{81} \; \dot{\zeta}_{82}]^T = \begin{bmatrix} \mu_8(f_8 + g_8 u_8 - \rho_8 - \chi_{72} - \dot{\xi}_{72}) \\ -\mu_8 k_{82}\zeta_{81} \end{bmatrix},
\tag{73}
$$

where $\mu_7 = k_7 + \frac{1}{2}|s_7|^{-1/2}$ and $\mu_8 = k_8 + \frac{1}{2}|s_8|^{-1/2}$. We can select the virtual control α_7 for recursive input and control input u_4 as follows:

$$
\alpha_7 = -k_{71}\zeta_{71} - k_{71}\xi_{71} - \beta_{\xi,71}sig^{1/2}(\xi_{71}) + \dot{x}_{7d} + \zeta_{72},
\tag{74}
$$

$$
u_4 = u_\psi = \frac{1}{g_8}(-k_{81}\zeta_{81} - k_{81}\xi_{81} - f_8 + \hat{\rho}_8 + \chi_{72} - \xi_{71} - \beta_{\xi,81}sig^{1/2}(\xi_{82}) - \frac{\varsigma_7\eta_7}{\varsigma_8\eta_8}s_8 + \zeta_{82}).
\tag{75}
$$

We define the Lyapunov function candidate as follows:

$$
V_3 = \frac{1}{2}\zeta_7^T P_7 \zeta_7 + \frac{1}{2}\zeta_8^T P_8 \zeta_8,
\tag{76}
$$

where P_k denotes positive definite matrices defined with $c_k > 0$ and $\varepsilon_k > 0$ as follows:

$$
P_k = \begin{bmatrix} c_k + 4\varepsilon_k^2 & -2\varepsilon_k \\ -2\varepsilon_k & 1 \end{bmatrix}, k = 7, 8.
$$

Substituting (74) and (75) into (72) and (73), respectively, and differentiating (76) with respect to time results in the following expression:

$$
\dot{V}_3 = \zeta_7^T P_7 \dot{\zeta}_7 + \zeta_8^T P_8 \dot{\zeta}_8 \le -\mu_7 \zeta_7^T Q_7 \zeta_7 + \mu_7\mu_7 s_8 - \mu_8 \zeta_8^T Q_8 \zeta_8 - \mu_7\eta_7 s_7 + \tilde{\rho}_8^T \chi_8 \eta_8,
$$
$$
\le -\sum_{k=7}^{8} \mu_k \zeta_k^T Q_k \zeta_k + \delta_8,
\tag{77}
$$

where $\eta_k = (c_k + 4\varepsilon_k^2)\zeta_{k1} - 2\varepsilon_k\zeta_{k2}$, $|\tilde{\rho}_8^T \mu_8\eta_8| \le \delta_8$, and the positive definite matrix

$$
Q_k = \begin{bmatrix} 2k_{k1}(c_k + 4\varepsilon_k^2) - 4k_{k2}\varepsilon_k & (c_k + 4\varepsilon_k^2) - 2\varepsilon_k k_{k1} + k_{k2} \\ c_k + 4\varepsilon_k^2 - 2\varepsilon_k k_{k1} + k_{k2} & 4\varepsilon_k \end{bmatrix}, k = 7, 8.
$$

3.4. Design of the Disturbance Observer

Assumption 1. *The disturbance $|\rho(t)|$ is bounded such that there exists an unknown constant that satisfies $|\rho(t)| \leq \bar{\rho}$.*

Theorem 4. *The disturbances $\rho = [\rho_2\ \rho_4\ \rho_6\ \rho_8]^T$ are estimated by the following novel nonlinear disturbance observers:*

$$\dot{\hat{\Theta}} = \mu_2[f(x) + gu - \chi_2 - \dot{\xi}_2 - \hat{\rho}],$$
$$\dot{\hat{\rho}} = -\Lambda^2[\eta_{\rho1}\sinh(c_{\rho1}\varphi_1(\widetilde{\Theta})) + \eta_{\rho2}\sinh(c_{\rho2}\Lambda^{-1}\varphi_2(\hat{\rho}))], \tag{78}$$

where $\Theta = [\zeta_{21}\ \zeta_{41}\ \zeta_{61}\ \zeta_{81}]^T$ denotes the state vector, including the super-twisting state vector, $\mu_2 = diag(\mu_2, \mu_4, \mu_6, \mu_8)$, $\chi_2 = [\chi_{12}\ \chi_{32}\ \chi_{52}\ \chi_{72}]^T$ denotes the state vector of the tracking differentiator, $\dot{\xi}_2 = [\dot{\xi}_{12}\ \dot{\xi}_{32}\ \dot{\xi}_{52}\ \dot{\xi}_{72}]^T$ denotes the state vector of the compensating signal, $\varphi_1(\widetilde{\Theta}) = \kappa sig^{1/2}(\widetilde{\Theta}) + (1-\kappa)sig^{(2+\gamma)/2}(\widetilde{\Theta})$, $\varphi_2(\hat{\rho}) = sig^{1/2}(\hat{\rho})$, $\widetilde{\Theta} = \Theta - \hat{\Theta}$, $\widetilde{\rho} = \rho - \hat{\rho}$, $\hat{\Theta}$ and $\hat{\rho}$ denote the estimates of Θ and ρ, Λ, $\eta_{\rho1}$, $\eta_{\rho2}$, $c_{\rho1}$, and $c_{\rho1}$ are diagonal positive constant matrices, respectively. Evidently, $\hat{\Theta} \to \Theta$ and $\hat{\rho} \to \rho$ when $\Lambda \to \infty$.

Proof. When $\Lambda \to \infty$, $\left|\dot{\hat{\rho}}\right| = \left|\Lambda^2[\eta_{\rho1}\sinh(c_{\rho1}\varphi_1(\widetilde{\Theta})) + \eta_{\rho2}\sinh(c_{\rho2}\Lambda^{-1}\varphi_2(\hat{\rho}))]\right|$ can be assumed as an infinitely large value. This indicates that the variation in $\hat{\rho}$ significantly exceeds $f(x) + gu - \chi_2 - \dot{\xi}_2$. Furthermore, it suggests that $\lim\limits_{\Lambda \to \infty} \frac{d(f(x)+gu-\chi_2-\dot{\xi}_2+\hat{\rho})}{dt} = \dot{\hat{\rho}}$, $\lim\limits_{\Lambda \to \infty} \Lambda^{-1}(f(x) + gu - \chi_2 - \dot{\xi}_2 + \hat{\rho}) = \Lambda^{-1}\hat{\rho}$. Hence, it is easy to note that (78) holds according to Theorem (1) when $\mu_2[f(x) + gu - \chi_2 - \dot{\xi}_2 + \hat{\rho}]$ is considered as $\hat{\Theta}$. This concludes the proof. □

To compare of the proposed observer with the conventional observers, two disturbance observers were provided. The first observer is designed using the structure of the tracking differentiator proposed by Zong et al. [28,29] expressed in (20) as follows:

$$\dot{\hat{\Theta}} = \mu_2[f(x) + gu - \chi_2 - \dot{\xi}_2 + \hat{\rho}],$$
$$\dot{\hat{\rho}} = -\Lambda^2[\eta_{\rho1}\{\widetilde{\Theta} + \left|\widetilde{\Theta}\right|^\beta tansig(c_{\rho1}\widetilde{\Theta})\} + \eta_{\rho2}\{\hat{\rho}\Lambda^{-1} + \left|\hat{\rho}\Lambda^{-1}\right|^\beta tansig(c_{\rho2}\hat{\rho}\Lambda^{-1})\}]. \tag{79}$$

The second observer is designed using the structure of the tracking differentiators proposed by Levant [30,31] expressed in (21) as follows:

$$\dot{\hat{\Theta}} = \mu_2[f(x) + gu - \chi_2 - \dot{\xi}_2 + \hat{\rho} - r_1 sig^{1/2}(\widetilde{\Theta})],$$
$$\dot{\hat{\rho}} = -r_2 sign(\widetilde{\Theta}). \tag{80}$$

4. Stability Analysis

Lemma 1. ([50]). *Consider the system $\dot{x} = f(x)$. For the given positive scalar constants, c_1, c_2, $0 < \gamma < 1$, and δ, if the continuous function $V(x)$ satisfies $\dot{V}(x) \leq -c_1 V(x) - c_2 V^\gamma(x) + \delta$, then the trajectory of the system $\dot{x} = f(x)$ is finite time stable and convergence time is bounded as follows:*

$$T_s \leq \max[t_0 + \frac{1}{vc_1(1-\gamma)} \ln \frac{vc_1 V^{1-\gamma}(t_0) + c_2}{c_2},$$
$$t_0 + \frac{1}{c_1(1-\gamma)} \ln \frac{c_1 V^{1-\gamma}(t_0) + vc_2}{vc_2}]. \tag{81}$$

Theorem 5. *If the sliding mode surfaces are defined as (23), (24), (43)–(46), (66), and (67), then systems (7)–(12) are controlled by virtual controls (33), (57), (58), (74) and control inputs (34), (59), (60), (75), and the unknown disturbances are estimated by the nonlinear disturbance observer provided in (78). Furthermore, the equilibrium points of (7)–(12) are asymptotically stable, and the trajectory of the closed-loop signals is bounded in finite time as follows:*

$$\lim_{t \to T_s} V(\zeta) \le \min \left\{ \frac{\Delta}{(1-v)\Lambda_{1\min}}, \left(\frac{\Delta}{(1-v)\Lambda_{2\min}} \right)^{1/2} \right\}$$

$$T_s \le \max\left[t_0 + \frac{2}{v\Lambda_{1\min}} \ln \frac{v\Lambda_{1\min}V^{1/2}(t_0)+\Lambda_{2\min}}{\Lambda_{2\min}}, t_0 + \frac{2}{\Lambda_{1\min}} \ln \frac{\Lambda_{1\min}V^{1/2}(t_0)+v\Lambda_{2\min}}{v\Lambda_{2\min}} \right] \tag{82}$$

if the parameter conditions guarantee positive definiteness of Q_k, i.e.,

$$k_{k1} > \frac{2\varepsilon_k^3}{c_k} + \frac{c_k}{8} + \varepsilon_k, k_{k2} > 2\varepsilon_k k_{k1}. \tag{83}$$

Proof. By defining the Lyapunov function as $V = \sum_{k=1}^{3} V_k$ using the results from (39), (63), and (76), we can obtain the following expression:

$$\dot{V} \le -\sum_{k=1}^{8} \mu_k \zeta_k^T Q_k \zeta_k + \sum_{k=1}^{4} \delta_{2k}. \tag{84}$$

Given that

$$\frac{1}{2}\lambda_{\min}(P_k)\|\zeta_k\|^2 \le \frac{1}{2}\zeta_k^T P_k \zeta_k \le \frac{1}{2}\lambda_{\max}(P_k)\|\zeta_k\|^2, \tag{85}$$

$$\frac{1}{2^{1/2}}\lambda_{\min}^{1/2}(P_k)\|\zeta_k\| \le V_k^{1/2} \le \frac{1}{2^{1/2}}\lambda_{\max}^{1/2}(P_k)\|\zeta_k\|, \tag{86}$$

and $\|\zeta_k\| = \left(\zeta_{k1}^2 + \zeta_{k2}^2\right)^{1/2} = \left(k_{k1}^2 s_k^2 + 2k_{k1}|s_k|^{3/2} + |s_k| + s_{k2}^2\right)^{1/2}$, and $|s_k|^{-1/2} \le |s_k| \le \|s_k\| \le \frac{2^{1/2}V_k^{1/2}}{\lambda_{\min}^{1/2}(P_k)}$, then

$$\dot{V} \le -\sum_{k=1}^{8} \mu_k \zeta_k^T Q_k \zeta_k + \Delta$$

$$\le -\sum_{k=1}^{8} \lambda_{\min}(Q_k)\left(k_{k1} + \frac{1}{2}|s_{k1}|^{-1/2}\right)\|\zeta_k\|^2 + \Delta$$

$$= -\sum_{k=1}^{8} k_{k1}\lambda_{\min}(Q_k)\|\zeta_k\|^2 - \frac{1}{2}\sum_{k=1}^{8} \frac{\lambda_{\min}(Q_k)}{|s_{k1}|^{-1/2}}\|\zeta_k\|^2 + \Delta \tag{87}$$

$$\le -2\sum_{k=1}^{8} k_{k1}\frac{\lambda_{\min}(Q_k)}{\lambda_{\max}(P_k)}V_k - \frac{1}{2^{1/2}}\sum_{k=1}^{8} \frac{\lambda_{\min}(Q_k)\lambda_{\min}^{1/2}(P_k)}{\lambda_{\max}(P_k)}V_k^{-1/2} + \Delta$$

$$\le -\sum_{k=1}^{8} \Lambda_{k1}V_k - \sum_{k=1}^{8} \Lambda_{k2}V_k^{-1/2} + \Delta \le -\Lambda_{1\min}V - \Lambda_{2\min}V^{1/2} + \Delta,$$

where $\Delta = \sum_{k=1}^{4} \delta_{2k}$, $\Lambda_{2\min} = \min(\Lambda_{k2})$, $\Lambda_{1\min} = \min(\Lambda_{k1})$ $\Lambda_1 = 2k_{k1}\frac{\lambda_{\min}(Q_k)}{\lambda_{\max}(P_k)}$, and $\Lambda_{k2} = \frac{1}{2^{1/2}}\frac{\lambda_{\min}(Q_k)\lambda_{\min}^{1/2}(P_k)}{\lambda_{\max}(P_k)}$. Then, (74) is expressed as follows:

$$\dot{V} \le -v\Lambda_{1\min}V - (1-v)\Lambda_{1\min}V - \Lambda_{2\min}V^{1/2} + \Delta \tag{88}$$

or

$$\dot{V} \le -\Lambda_{1\min}V - v\Lambda_{2\min}V^{1/2} - (1-v)\Lambda_{2\min}V^{1/2} + \Delta \tag{89}$$

given that $V \geq \frac{\Delta}{(1-v)\Lambda_{1\min}}$, we obtain the following expression:

$$\dot{V} \leq -v\Lambda_{1\min}V - \Lambda_{2\min}V^{1/2}. \tag{90}$$

From Lemma 1, the boundedness of $V(\zeta)$ decreases argument ζ

$$\zeta \in \left\{ V(\zeta) \leq \frac{\Delta}{(1-v)\Lambda_{1\min}} \right\}. \tag{91}$$

Thus, the convergence time T_s is given as follows:

$$T_s \leq t_0 + \frac{2}{v\Lambda_{1\min}} \ln \frac{v\Lambda_{1\min}V^{1/2}(t_0) + \Lambda_{2\min}}{\Lambda_{2\min}}. \tag{92}$$

Next, given that $V \geq \frac{\Delta}{(1-v)\Lambda_{2\min}}$, we obtain the following expression:

$$\dot{V} \leq -\Lambda_{1\min}V - v\Lambda_{2\min}V^{1/2}. \tag{93}$$

This leads to the following:

$$\zeta \in \left\{ V^{1/2}(\zeta) \leq \frac{\Delta}{(1-v)\Lambda_{2\min}} \right\}, \tag{94}$$

$$T_s \leq t_0 + \frac{2}{\Lambda_{1\min}} \ln \frac{\Lambda_{1\min}V^{1/2}(t_0) + v\Lambda_{2\min}}{v\Lambda_{2\min}}. \tag{95}$$

Therefore, $V(\zeta)$ is a continuously decreasing strong Lyapunov function, and the equilibrium point $\zeta = 0$ is reached in finite time from every initial condition. This also guarantees that the equilibrium point $s = 0$ is reached in finite time from every initial condition. This concludes the proof. $\square$

Theorem 6. *The finite time convergence of the compensating dynamics given in (25), (47), and (68) is also guaranteed by the finite time convergence of ξ_{ij}. Thus, the finite time boundedness of ξ_{ij} is demonstrated by defining the following expression:*

$$V_{\xi} = \sum_{j=1}^{2} \frac{1}{2}\xi_{1j}^2 + \sum_{j=1}^{2} \frac{1}{2}\xi_{3j}^2 + \sum_{j=1}^{2} \frac{1}{2}\xi_{5j}^2 + \sum_{j=1}^{2} \frac{1}{2}\xi_{7j}^2. \tag{96}$$

The convergence time $T_{\xi r}$ is then obtained as

$$T_{\xi r} \leq \frac{4V_{\xi}^{1/4}(0)}{\lambda\Xi_{\xi}}. \tag{97}$$

Proof. From (96), one can obtain that

$$
\begin{aligned}
\dot{V}_\xi &= \sum_{j=1}^{2} \xi_{1j}\dot{\xi}_{1j} + \sum_{j=1}^{2} \xi_{3j}\dot{\xi}_{3j} + \sum_{j=1}^{2} \xi_{5j}\dot{\xi}_{5j} + \sum_{j=1}^{2} \xi_{7j}\dot{\xi}_{7j} \\
&= \xi_{11}[-k_{11}\xi_{11} + \xi_{12} + \chi_{11} - \alpha_1 - \beta_{\zeta,11}sig^{1/2}(\xi_{11})] \\
&\quad + \xi_{12}[-k_{12}\xi_{12} - \xi_{11} - \beta_{\zeta,12}sig^{1/2}(\xi_{12})] + \\
&\quad \cdots + \xi_{71}[-k_{71}\xi_{71} + \xi_{72} + \chi_{71} - \alpha_7 - \beta_{\zeta,71}sig^{1/2}(\xi_{71})] \\
&\quad + \xi_{72}[-k_{72}\xi_{72} - \xi_{71} - \beta_{\zeta,72}sig^{1/2}(\xi_{72})] \\
&\leq -\sum_{j=1}^{2} k_{1j}^2\xi_{1j}^2 - \sum_{j=1}^{2} k_{3j}^2\xi_{3j}^2 - \sum_{j=1}^{2} k_{5j}^2\xi_{5j}^2 - \sum_{j=1}^{2} k_{7j}^2\xi_{7j}^2 \\
&\quad - \sum_{j=1}^{2} \beta_{\xi,1j}|\xi_{1j}|^{3/2} - \sum_{j=1}^{2} \beta_{\xi,3j}|\xi_{3j}|^{3/2} \\
&\quad - \sum_{j=1}^{2} \beta_{\xi,5j}|\xi_{5j}|^{3/2} - \sum_{j=1}^{2} \beta_{\xi,1j}|\xi_{1j}|^{3/2} + |\xi_{11}||\zeta_{11} - \alpha_{11}| + |\xi_{31}||\zeta_{31} - \alpha_{31}| \\
&\quad + |\xi_{51}||\zeta_{51} - \alpha_{51}| + |\xi_{71}||\zeta_{71} - \alpha_{71}| \\
&\leq -\sum_{j=1}^{2} k_{1j}^2\xi_{1j}^2 - \sum_{j=1}^{2} k_{3j}^2\xi_{3j}^2 - \sum_{j=1}^{2} k_{5j}^2\xi_{5j}^2 - \sum_{j=1}^{2} k_{7j}^2\xi_{7j}^2 \\
&\quad - \sum_{j=1}^{2} \beta_{\xi,1j}|\xi_{1j}|^{3/2} - \sum_{j=1}^{2} \beta_{\xi,3j}|\xi_{3j}|^{3/2} \\
&\quad - \sum_{j=1}^{2} \beta_{\xi,5j}|\xi_{5j}|^{3/2} - \sum_{j=1}^{2} \beta_{\xi,1j}|\xi_{1j}|^{3/2} + \delta_{11}|\xi_{11}| + \delta_{31}|\xi_{31}| \\
&\quad + \delta_{51}|\xi_{51}| + \delta_{71}|\xi_{71}| \leq -(k_{11}^2 - \tfrac{1}{2})\xi_{11}^2 - (k_{31}^2 - \tfrac{1}{2})\xi_{31}^2 - (k_{51}^2 - \tfrac{1}{2})\xi_{51}^2 \\
&\quad - (k_{71}^2 - \tfrac{1}{2})\xi_{71}^2 - k_{12}^2\xi_{12}^2 - k_{32}^2\xi_{32}^2 - k_{52}^2\xi_{52}^2 - k_{72}^2\xi_{72}^2 \\
&\quad - \sum_{j=1}^{2} \beta_{\xi,1j}|\xi_{1j}|^{3/2} - \sum_{j=1}^{2} \beta_{\xi,3j}|\xi_{3j}|^{3/2} - \sum_{j=1}^{2} \beta_{\xi,5j}|\xi_{5j}|^{3/2} - \sum_{j=1}^{2} \beta_{\xi,1j}|\xi_{1j}|^{3/2} + \Delta,
\end{aligned}
\tag{98}
$$

where $\Delta = \frac{1}{2}(\delta_{11}^2 + \delta_{31}^2 + \delta_{51}^2 + \delta_{71}^2)$ and $|\zeta_{i,1} - \alpha_{i,1}| \leq \delta_{i,1}$ can be achieved in finite time. Then, (98) is expressed under the condition of $k_{i,1}^2 \geq \frac{1}{2}$ as

$$
\begin{aligned}
\dot{V}_\xi &\leq -\sum_{j=1}^{2} \beta_{\xi,1j}|\xi_{1j}|^{3/2} - \sum_{j=1}^{2} \beta_{\xi,3j}|\xi_{3j}|^{3/2} - \sum_{j=1}^{2} \beta_{\xi,5j}|\xi_{5j}|^{3/2} \\
&\quad - \sum_{j=1}^{2} \beta_{\xi,1j}|\xi_{1j}|^{3/2} + \Delta \\
&\leq -\Xi_\xi V_\xi^{3/4} + \Delta,
\end{aligned}
\tag{99}
$$

with $\Xi_\xi = \min[2^3\beta_{\xi i,j}]$, $i = 1, 3, 5, 7$, $j = 1, 2$. Then, (99) is expressed as follows:

$$
\dot{V}_\xi \leq -\lambda\Xi_\xi V_\xi^{3/4} - (1 - \lambda)\Xi_\xi V_\xi^{3/4} + \Delta,
\tag{100}
$$

under the condition that there exists a scalar $0 < \lambda < 1$. If $V_\xi^{3/4} \geq \frac{\Delta}{(1-\lambda)\Xi_\xi}$ is satisfied, (100) is expressed as follows:

$$
\dot{V}_\xi \leq -\lambda\Xi_\xi V_\xi^{3/4}.
\tag{101}
$$

Consequently, $V_\xi(t)$ approaches zero in finite time, and the finite time convergence of $\xi_{i,j}$ is guaranteed. The convergence time $T_{\xi r}$ is obtained as follows:

$$
T_{\xi r} \leq \frac{4V_\xi^{1/4}(0)}{\lambda\Xi_\xi}.
\tag{102}
$$

This concludes the proof. □

5. Simulation Results

In this section, simulations for three cases, including the nominal system, perturbed system without the observer, and perturbed system with the observer are conducted to evaluate the performance of the proposed controller and disturbance observer for the hexacopter UAV system. Four control systems were designed to compare the proposed scheme with the conventional methods: namely, the standard BSC system (BSC); Levant's tracking differentiator [31,32] based BSC system (YTBSC) studied by Yu et al. [50]; Zong's tracking differentiator [28,29] based BSC system (ZTBSC), where the adopted controller is designed according to those in [50]; and proposed tracking differentiator and super-twisting algorithm based BSC system (PTSBSC). The system parameters of the hexacopter UAV are listed in Table 1 of [10].

Table 1. Selected values of the hexacopter UAV.

Symbol	Quantity	Value
m_0	nominal mass of the body	1.5 kg
l	length of arm	0.275 m
J_x, J_y, J_z	moment of inertia at each axis	3.259×10^{-2}, 3.259×10^{-2}, 6.059×10^{-2} kg $\cdot$ m^2
J_r	moment of inertia at propeller	9.9×10^{-5} kg $\cdot$ m^2
C_d	coefficient of drag	1.523×10^{-7} Nms^2

To compare the performance of the tracking differentiators presented in Section 2, the parameters are selected as $R = 2$, $r_1 = 1.5$, $r_2 = 5.5$, $a_1 = 1$, $a_2 = 0.5$, $\beta = 0.5$, $\gamma = 0.5$ and $\kappa = 0.95$ under the initial condition of $\alpha = 0$, $x_1(0) = 2$, and $x_2(0) = -2$. Comparative results are presented in Figure 2, where the proposed differentiator shows more rapid convergence performance than others. Only three tracking differentiators are considered, excluding the tracking differentiator proposed by Yang et al. [27] due to its lower performance.
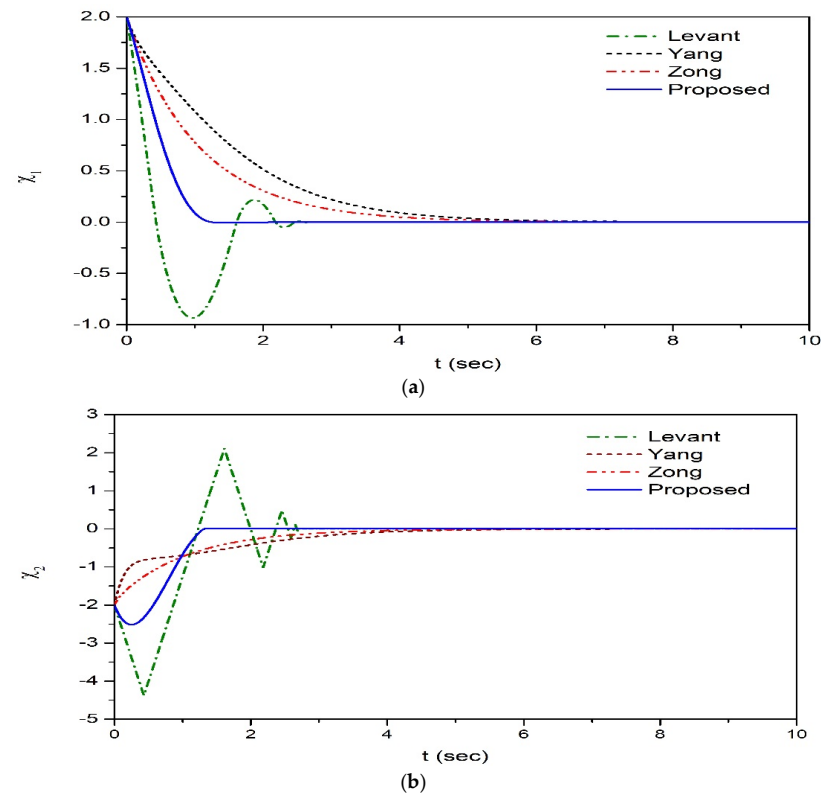

Figure 2. Comparative results for three tracking differentiators. (**a**) χ_1. (**b**) χ_2.

5.1. Simulation Results of the Nominal Hexacopter USV System

The design parameters of the controller and observer are selected via the trial-and-error method. The selected values are listed in Tables 2–4.

Table 2. Selected values of the tracking differentiator.

Differentiator	Selected Value
Altitude	$R_1 = 20,\ r_{11} = 20,\ r_{12} = 20,\ a_{11} = 2,\ a_{12} = 2,\ \kappa_1 = 1.2$
Longitudinal and Lateral	$R_3 = 20,\ r_{31} = 20,\ r_{32} = 20,\ a_{31} = 2,\ a_{32} = 2,\ \kappa_3 = 1.2$
	$R_5 = 20,\ r_{51} = 5,\ r_{52} = 5,\ a_{51} = 1,\ a_{52} = 1,\ \kappa_5 = 1.2$
Heading	$R_7 = 20,\ r_{71} = 20,\ r_{72} = 20,\ a_{71} = 2,\ a_{72} = 2,\ \kappa_6 = 1.2$

Table 3. Selected values of the compensating signal.

Compensator	Selected Value
Altitude	$k_{11} = 0.5,\ k_{12} = 0.5,\ \beta_{\zeta,11} = 1,\ \beta_{\zeta,12} = 1$
Longitudinal and Lateral	$k_{31} = 0.5,\ k_{32} = 0.5,\ \beta_{\zeta,31} = 1,\ \beta_{\zeta,32} = 1$
	$k_{51} = 0.5,\ k_{52} = 0.5,\ \beta_{\zeta,51} = 0.5,\ \beta_{\zeta,52} = 0.5$
Heading	$k_{71} = 0.5,\ k_{72} = 0.5,\ \beta_{\zeta,71} = 0.1,\ \beta_{\zeta,72} = 0.1$

Table 4. Selected values of the disturbance observer.

Observer	Selected Value
Altitude	$\Lambda_z = 10,\ \eta_{\rho z1} = 0.1,\ \eta_{\rho z2} = 0.1, c_{\rho z1} = 2,\ c\eta_{\rho z2} = 2,\ \kappa_z = 1.2$
Longitudinal	$\Lambda_x = 15,\ \eta_{\rho x1} = 0.2,\ \eta_{\rho x2} = 0.2, c_{\rho x1} = 2,\ c\eta_{\rho x2} = 2,\ \kappa_x = 1.2$

The command trajectories of each axis were selected as follows:

$$x_d(t) = \begin{cases} 2\text{ m}, & 0 < t \leq 40 \\ 5\text{ m}, & 40 < t \leq 60 \\ 1\text{ m}, & 60 < t \leq 100 \end{cases}, y_d(t) = \begin{cases} 1\text{ m}, & 0 < t \leq 25 \\ 2.5\text{ m}, & 25 < t \leq 80 \\ 1.5\text{ m}, & 80 < t \leq 100 \end{cases}, z_d(t) = \begin{cases} 5\text{ m}, & 0 < t \leq 80 \\ 3\text{ m}, & 80 < t \leq 100 \end{cases},$$

$$\psi_d(t) = \begin{cases} 0\text{ rad}, & 0 < t \leq 28 \\ 0.25\text{ rad}, & 28 < t \leq 80 \\ 0.125\text{ rad}, & 80 < t \leq 100 \end{cases}, \phi_d(t) = 0\text{ rad},\ \theta_d(t) = 0\text{ rad}.$$

Simulation results for the nominal hexacopter system are shown in Figure 3, wherein the additional load mass and disturbances are not considered. The position tracking result in 3D space is shown in Figure 3a. The position tracking results for the translation axes are presented in Figure 3b–d. The angular position tracking results are shown in Figure 3e–g. To clarify the tracking performance for each control system, tracking errors for x, y, z, and ψ axes are shown in Figure 3i–l. As shown in Figure 3i,j, the tracking performances of the BSC and YTBSC are similar. As shown in Figure 3k, the improvement in the tracking performance of the z-axis of the YTBSC exceeds that of the BSC system. However, the performance of the PTSBSC system exceeds that of the other two systems as shown in Figure 3h–k. The control inputs of the altitude and heading controllers are shown in Figure 3l,m, respectively.
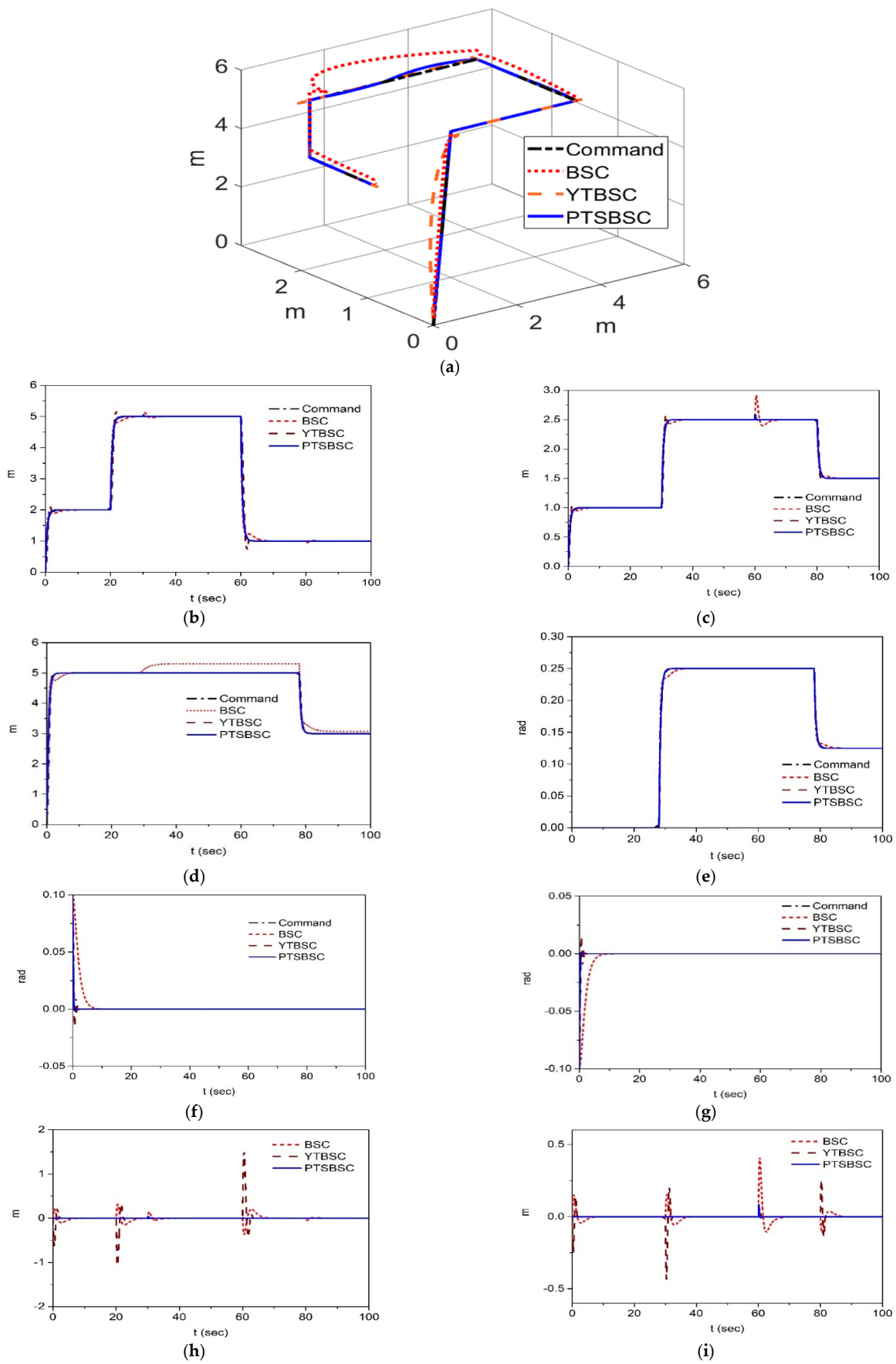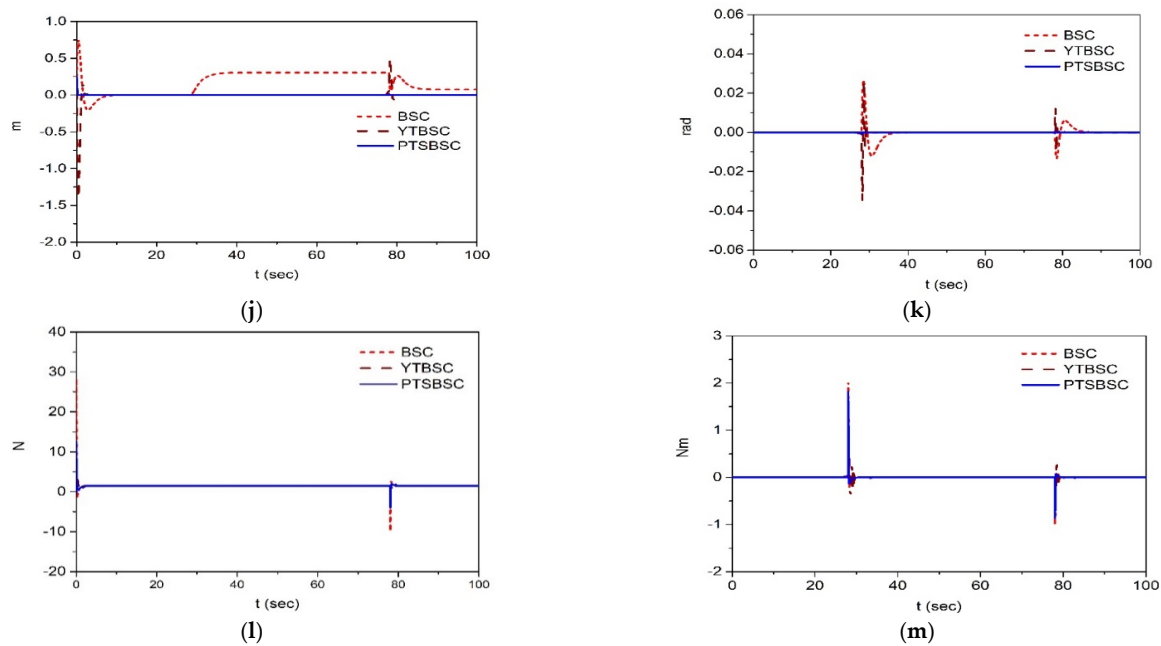
Figure 3. *Cont.*

(j)

(k)

(l)

(m)

Figure 3. Simulation results of the nominal hexacopter system. (**a**) The 3D tracking result. (**b**) Output of *x*-axis. (**c**) Output of *y*-axis. (**d**) Output of *z*-axis. (**e**) Output of ψ-axis. (**f**) Output of ϕ-axis. (**g**) Output of θ-axis. (**h**) Tracking error of *x*-axis. (**i**) Tracking error of *y*-axis. (**j**) Tracking error of *z*-axis. (**k**) Tracking error of ψ-axis. (**l**) Control input of latitude controller. (**m**) Control input of heading controller.

5.2. Simulation Results of the Perturbed System

Subsequently, simulation for the perturbed system with a 200% increase in the mass of the hexacopter, which denotes the variation in the load mass, is conducted to evaluate robustness with respect to the load perturbation. The other perturbations are as follows:

$$d_x = 0.1\,\mathrm{N\,s/m}, d_y = 0.01\,\mathrm{N\,s/m}, d_z = 0.1\,\mathrm{N\,s/m}, d_\phi = d_\theta = d_\psi = 0.012\,\mathrm{N\,s/rad}.$$

Additionally, the wind disturbance of $1.5\sin(t)\,\mathrm{m/s}^2$ is applied to the *x*-axis. The simulation results are shown in Figure 4, where the 3D tracking result is shown in Figure 4a and the tracking results in each axis are shown in Figure 4b–e. Outputs in the *x* and *y* axes of the conventional BSC system indicate high oscillation, and the latitude error exceeds those of other systems. The outputs of the YTBSC system exhibit high overshoot in the point of direction change as shown in Figure 4b–e. Conversely, the simulation results in Figure 4 indicate that the robustness of the proposed PTSBSC system exceeds those of the two systems for the disturbance due to mass variation and other disturbances.

5.3. Simulation Results of the Perturbed System with Disturbance Observer

Under the same disturbance conditions, as listed in Section 5.2, simulation for the perturbed system with the controller blended with the disturbance observers based on (78) (proposed), (79) (Zong [28,29]), and (80) (Levant [30,31]) is conducted to evaluate the estimation performance. The simulation results are shown in Figure 5, where the 3D tracking result is presented in Figure 4a and the tracking errors in the *x*, *y*, *z*, and ψ-axes are shown in Figure 5b–e. The results indicate that the tracking results of the control system with the proposed observer exhibit a more efficient performance than that of the controller with the Levant observer. The estimates of the observer states and disturbances of the proposed observer are shown in Figure 5f–i. Estimates of the observer states and disturbances of the Levant observer are shown in Figure 5j–m. Finally, estimates of the observer states and disturbances of the Levant observer are shown in Figure 5n–q. The simulation results indicate that the estimate performance of the proposed observer exceeds

that of the conventional Levant and Zong observers. Table 5 shows the root mean square (RMS) value of the tracking error of each system, where it is shown that the RMS value of the proposed system decreases until an average 7% of that of Levant's system.
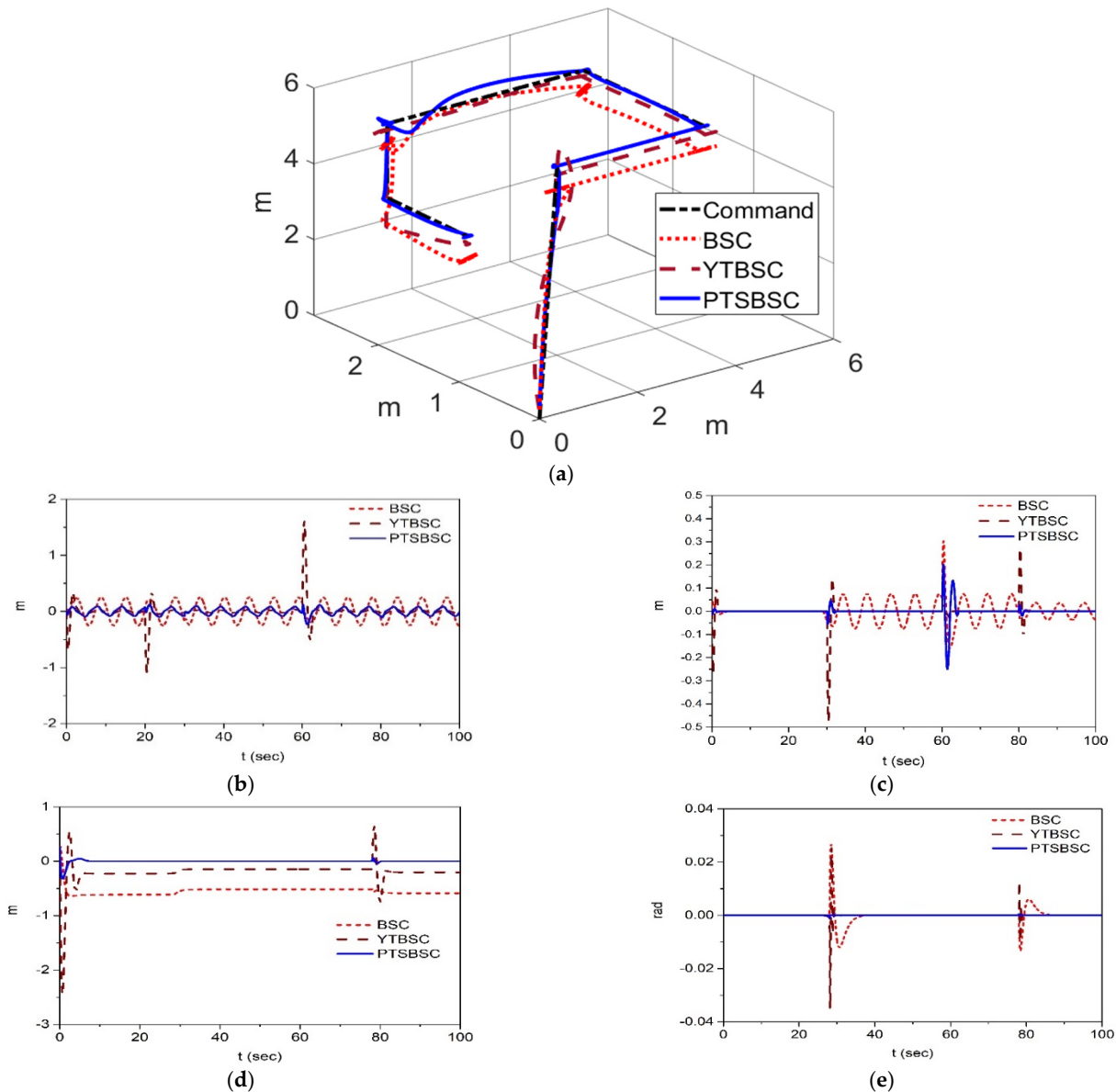

Figure 4. Simulation results of the perturbed hexacopter system. (**a**) 3D tracking result. (**b**) Tracking error for *x*-axis. (**c**) Tracking error for *y*-axis. (**d**) Tracking error for *z*-axis. (**e**) Tracking error for ψ-axis.

Table 5. RMS value of the tracking error of each system.

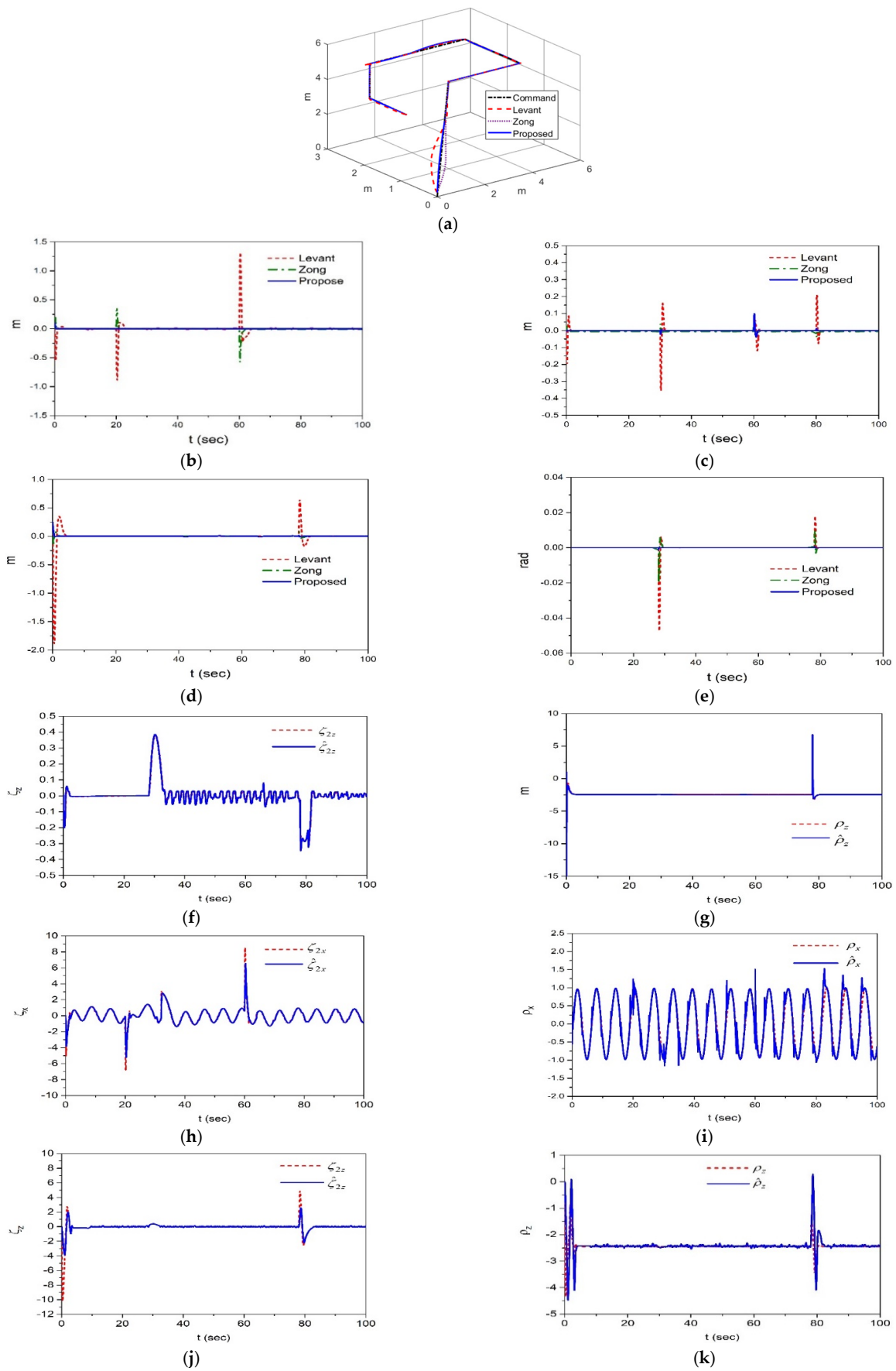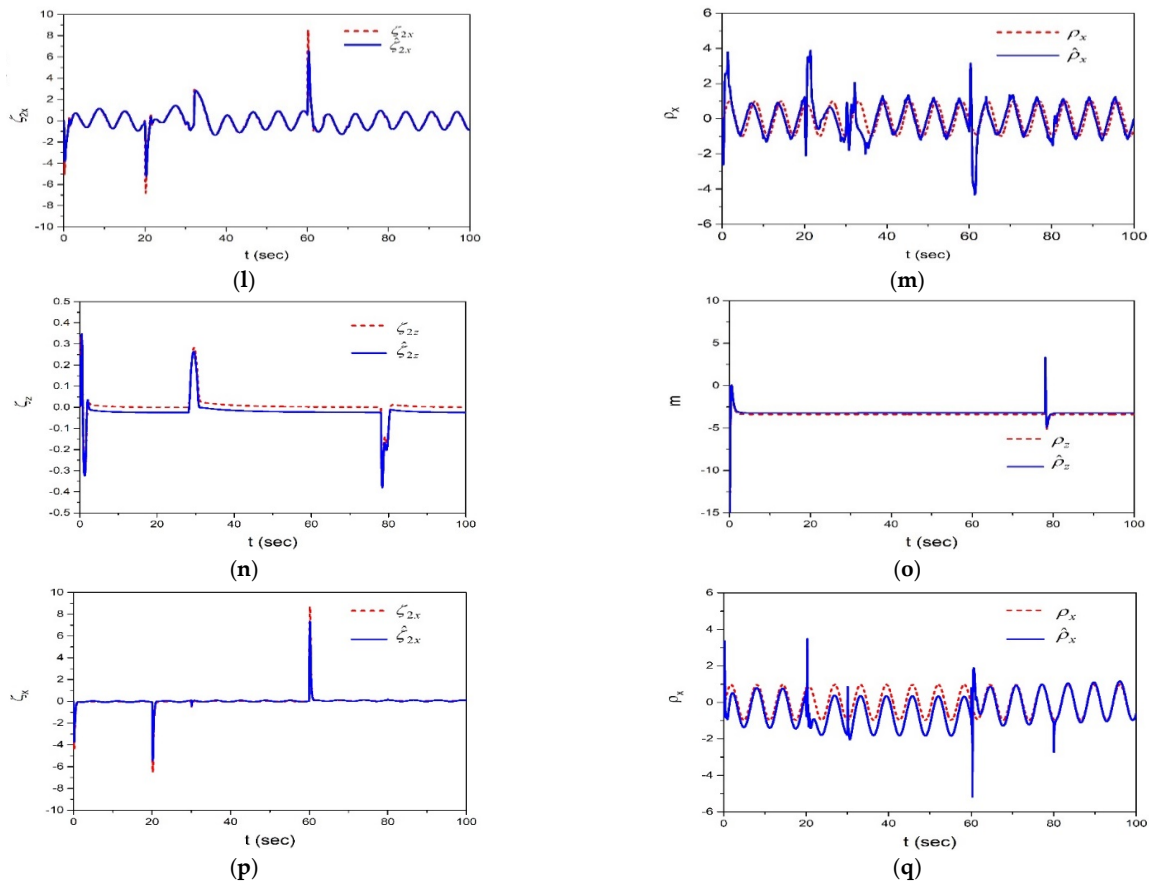| Axis	Levant	Zong	Proposed
x	0.108 (100%)	0.039 (36%)	0.006 (6%)
y	0.027 (100%)	0.007 (26%)	0.005 (19%)
z	0.155 (100%)	0.011 (7%)	0.008 (5%)
Average	0.097 (100%)	0.019 (20%)	0.006 (7%)

Figure 5. *Cont.*

Figure 5. Simulation results of the perturbed hexacopter system with the controller combined with the disturbance observer. (**a**) The 3D tracking result. (**b**) Tracking error for *x*-axis. (**c**) Tracking error for *y*-axis. (**d**) Tracking error for *z*-axis. (**e**) Tracking error for ψ-axis. (**f**) ζ_{2z} and $\hat{\zeta}_{2z}$ of the proposed observer. (**g**) ρ_z and $\hat{\rho}_z$ of the proposed observer. (**h**) ζ_{2x} and $\hat{\zeta}_{2x}$ of the proposed observer. (**i**) ρ_x and $\hat{\rho}_x$ of the proposed observer. (**j**) ζ_{2z} and $\hat{\zeta}_{2z}$ of the Levant observer. (**k**) ρ_z and $\hat{\rho}_z$ of the Levant observer. (**l**) ζ_{2x} and $\hat{\zeta}_{2x}$ of the Levant observer. (**m**) ρ_x and $\hat{\rho}_x$ of the Levant observer. (**n**) ζ_{2z} and $\hat{\zeta}_{2z}$ of the Zong observer. (**o**) ρ_z and $\hat{\rho}_z$ of the Zong observer. (**p**) ζ_{2x} and $\hat{\zeta}_{2x}$ of the Zong observer. (**q**) ρ_x and $\hat{\rho}_x$ of the Zong observer.

Finally, under the disturbance condition with the 300% increase in the mass and the same other condition, simulation for the perturbed system is conducted to evaluate the estimation performance with the disturbance observers based on (78) (proposed), (79) (Zong [28,29]), and (80) (Levant [30,31]). The desired 8-shape command trajectory is described as

$$\boldsymbol{P}_d(t) = \begin{bmatrix} x_d & y_d & z_d \end{bmatrix}^T = \begin{bmatrix} 0 & 0 & -4(1 - e^{-0.3t}) \end{bmatrix}^T \ (m), \ t \le 4s,$$

$$\boldsymbol{P}_d(t) = \begin{bmatrix} x_d \\ y_d \\ z_d \end{bmatrix} = \begin{bmatrix} 8 - 8\cos\left(\frac{2\pi(t-4)}{12}\right) \\ 4\sin\left(\frac{4\pi(t-4)}{12}\right) \\ -4(1 - e^{-0.3t}) \end{bmatrix}, \ t \ge 4s,$$

under other rotation commands set to be zero value.

In the first stage, the hexacopter UAV climbs vertically for 4 s to simulate the take-off flight. Next, it follows an 8-shaped path while continuing to lift. In the second stage, the lift, sideslip, and forward performances of the hexacopter UAV are evaluated comprehensively. The simulation results are shown in Figure 6, where the 3D tracking result is presented in Figure 6a, and the tracking output and errors in the *x*, *y*, *z* axes are shown in Figure 6b–g. The simulation results indicate that the tracking results of the control system with the proposed observer exhibit a more efficient performance than that of the controller with the

Levant observer, like the previous results. Table 6 shows the root mean square (RMS) value of the tracking error of each system, where it is shown that the RMS value of the proposed system decreases until an average 27% of that of Levant's system.
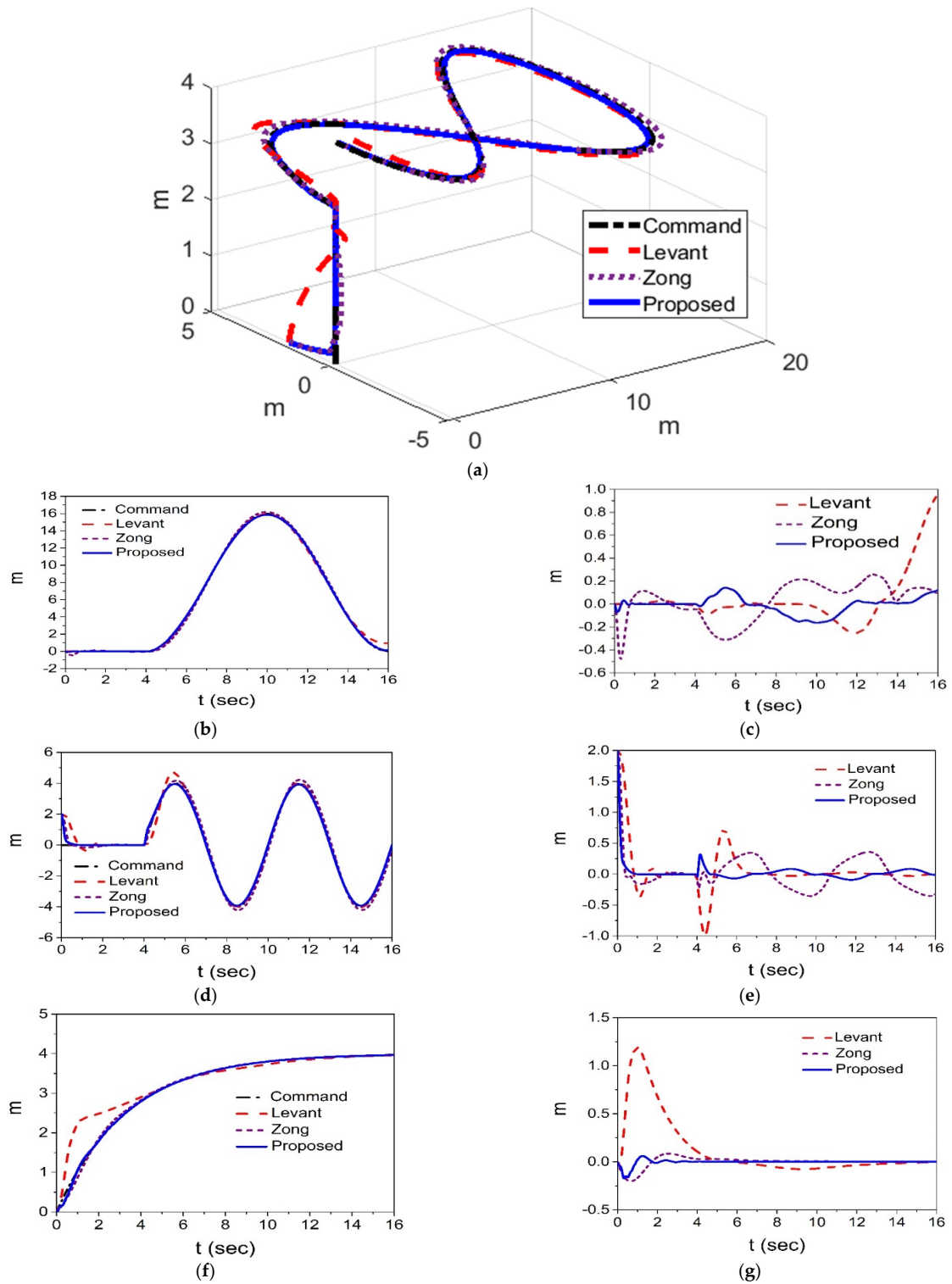

Figure 6. Simulation results of the perturbed hexacopter system for 300% increase in the mass with the controller combined with the disturbance observer. (**a**) The 3D tracking result. (**b**) Output of *x*-axis. (**c**) Tracking error of *x*-axis. (**d**) Output of *y*-axis. (**e**) Tracking error of *y*-axis. (**f**) Output of *z*-axis. (**g**) Tracking error of *z*-axis.

Table 6. RMS value of the tracking error of each system.

Axis	Levant	Zong	Proposed
x	0.231 (100%)	0.172 (75%)	0.074 (32%)
y	0.379 (100%)	0.294 (78%)	0.156 (41%)
z	0.344 (100%)	0.053 (15%)	0.028 (8%)
Average	0.318 (100%)	0.173 (54%)	0.086 (27%)

5.4. Discussions

Simulations are conducted for three cases, such as nominal system, perturbed system without disturbance observers, and perturbed system with disturbance observers. Simulation results of the nominal system for the linear position command trajectory show that the performance of the PTSBSC system exceeds that of the other BSC and YTBSC systems. This achievement is obtained, owing to the improved performance of the proposed tracking differentiator. The proposed tracking differentiator shows the best performance over the conventional tracking differentiators, including the recently developed ones.

The second simulation under the condition of the perturbation with wind gust and 200% increase in the mass is conducted to the control system without the disturbance observer. In this case, the control performance is only dependent on the property of the controller itself. The proposed PTSBSC system maintains the least performance variation compared with other two BSC and YTBSC systems, where a large variation of the output tracking results appears.

Finally, the disturbance observers are utilized to estimate uncertainties, such as the wind gust and 200% and 300% variations in the mass. Simulations are conducted for the linear position and 8-shaped command trajectories to evaluate various aspects of the control performance. The output performances are determined by the superiority of the adopted observer, where the proposed disturbance observer shows the outperforming estimation results. Therefore, the proposed control system with the novel disturbance observer is ascertained to provide the outperforming results compared to those of the traditional similar controller and disturbance observer systems.

In addition, the phenomenon of pilot-induced oscillations (PIOs) that represent a particular and specific aspect of the framework of human–machine interactions was and still is a dynamic behavior of great interest in the design of aircraft [51]. PIOs consists of sustained or uncontrollable oscillations, resulting from efforts of the pilot to control the aircraft. The disturbance problem of PIOs can occur also in controlling UAVs. However, the possibility to exploit strategies from nonlinear dynamics for controlling PIOs took fewer attention in the UAV control system. In this study, this type of disturbance was not considered yet. As a further study including an experimental examination, it is worth to explore this disturbance by the proposed nonlinear controller and disturbance observer to seek a more feasible control system under various aspects of real flight conditions of UAVs.

6. Conclusions

In this study, a super-twisting sliding mode backstepping control blended with a new tracking differentiator and disturbance observer based on the concept of the proposed tracking differentiator was examined to realize robust tracking control performance of a hexacopter UAV system. Recursive design in conventional backstepping control and faster convergence enabled the improved tracking differentiator to bypass the occurred repeated differentiation issue and obtain the continuous and smooth derivative of the virtual control. Next, the enhanced disturbance observer was designed to estimate uncertainties of the hexacopter UAV system based on the proposed tracking differentiator. Thus, the robust nonlinear controller equipped with the improved disturbance observer was designed to obtain a hexacopter UAV control system that outperforms the conventional control scheme in conditions with high nonlinearities and unknown disturbances. Sequential comparative simulations for the hexacopter nonlinear UAV system in a nominal case and a case with

variation in the load mass and wind disturbance were executed, and the simulation results demonstrated the efficiency of the proposed control system.

Nomenclature

symbol	name
a_i	coefficient of the tracking differentiator
α_i	virtual control
β_i	coefficient of the tracking differentiator
$\beta_{\xi,i}$	coefficient of the controller
δ_i	upper bound of the unknown uncertainty
η_i	auxiliary variable of the super-twisting state variable
ζ_i	super-twisting state variable and vector
$\tilde{\xi}_i$	state variable of the compensating signal system
$k_i, \Lambda_i, \kappa_i, \gamma_i$	design constants
r_i	coefficient of the tracking differentiator
R_i	coefficient of the tracking differentiator
ρ_i	lumped uncertainty
P_i, Q_i	positive definite matrices
$\varphi_i(\cdot)$	composite sig$(\cdot)$ function
s_i	sliding mode surface
u_i	controller

References

1. Chao, H.Y.; Cao, Y.; Chen, Y. Autopilots for small unmanned aerial vehicles: A survey. *Int. J. Control. Autom. Syst.* **2010**, *8*, 36–44. [CrossRef]
2. Cai, G.; Dias, J.; Senevirantne, L. A survey of small-scale unmanned aerial vehicles: Recent advances and future development trends. *Unmanned Syst.* **2014**, *2*, 1–25. [CrossRef]
3. Becerra, V.M. Autonomous control of unmanned aerial vehicles. *Electronics* **2019**, *8*, 1–5. [CrossRef]
4. Jasim, O.A.; Veres, S.M. A robust controller for multi rotor UAVs. *Aerosp. Sci. Tech.* **2020**, *105*, 1–14. [CrossRef]
5. Alaimo, A.; Artale, V.; Milazzo, C.; Ricciardello, C.; Trefiletti, L. Mathematical modeling and control of a hexacopter. In Proceedings of the 2013 International Conference on Unmanned Aircraft Systems (ICUAS), Atlanta, GA, USA, 28–31 May 2013; pp. 1043–1050.
6. Arellano-Muro, C.A.; Luque-Vega, L.; Castillo-Toledo, B.; Loukianov, A.G. Backstepping control with sliding mode estimation for a Hexacopter. In Proceedings of the 2013 10th International Conference on Electrical Engineering, Computing Science and Automatic Control (CCE), Mexico City, Mexico, 30 September 2013; pp. 31–36.
7. Alaimo, A.; Artale, V.; Milazzo, C.L.R.; Riccardello, A. PID controller applied to hexacopter flight. *J. Intell Robot Sys.* **2014**, *73*, 261–270. [CrossRef]
8. Nguyen, N.P.; Mung, N.X.; Hong, S.K. Actuator fault detection and fault-tolerant control for hexacopter. *Sensors* **2019**, *19*, 2–19. [CrossRef]

9.　Rosales, C.; Soria, C.M.; Rossomando, F.G. Identication and adaptive PID control of a hexacopeter UAV based on neural networks. *Int. J. Adapt. Signal Process.* **2019**, *33*, 74–91. [CrossRef]

10.　Zhang, J.; Gu, D.; Deng, C.; Wen, B. Robust and adaptive backstepping control for hexacopter UAVs. *IEEE Access* **2019**, *7*, 163502–163514. [CrossRef]

11.　Garcia, R.A.; Rubio, F.R.; Ortega, M.G. Robust PID control of the quadrotor helicopter. *IFAC Proc. Vol.* **2012**, *45*, 229–234. [CrossRef]

12.　Rinaldi, F.; Chiesa, S.; Quagliotti, F. Linear quadratic control for quadrotors UAVs dynamics and formation flight. *J. Intell. Robot. Syst.* **2013**, *70*, 203–220. [CrossRef]

13.　Khatoon, S.; Gupta, D.; Das, L.K. PID & LQR control for a quadrotor: Modeling and simulation. In Proceedings of the 2014 International Conference on Advances in Computing, Communications and Informatics (ICACCI), Delhi, India, 24 September 2014; pp. 796–802.

14.　Abdolhosseini, M.; Zhang, Y.; Rabbath, C. An efficient model predictive control scheme for an unmanned quadrotor helicopter. *J. Intell. Robot. Syst.* **2013**, *70*, 27–38. [CrossRef]

15.　Kang, T.; Yoon, K.; Ha, T.; Lee, G. H-infinity control system design for a quad-rotor. *J. Inst. Control Robot. Syst.* **2015**, *21*, 14–20. [CrossRef]

16.　Kristic, M.; Kanellakopoulos, I.; Kokotovic, P.V. *Nonlinear and Adaptive Control Design*; Wiley: New York, NY, USA, 1995.

17.　Li, Y.; Tong, S. Command-filtered-based fuzzy adaptive control design for MIMO-switched nonstrict-feedback nonlinear systems. *IEEE Trans. Fuzzy Syst.* **2017**, *25*, 668–680. [CrossRef]

18.　Mian, A.A.; Daobo, W. Modeling and backstepping-based nonlinear control strategy for a 6DOF quadrotor helicopeter. *Chin. J. Aeronaut.* **2008**, *21*, 261–268. [CrossRef]

19.　Das, A.; Lewis, F.; Subbaro, K. Backstepping approach for controlling a quadrotor using Lagrange form dynamics. *J. Intell. Robot. Syst.* **2009**, *56*, 127–151. [CrossRef]

20.　Ha, C.; Zuo, Z.; Choi, F.; Lee, D. Passitivity-based adaptive backstepping control of quadrotor-type UAVs. *Robot. Auton. Syst.* **2014**, *62*, 1305–1315. [CrossRef]

21.　Huo, X.; Huo, M.; Karimi, H.R. Attitude stabilization control of a quadrotor UAV by using backstepping approach. *Math. Probl. Eng.* **2014**, *2014*, 749803. [CrossRef]

22.　Basri, M.A.M.; Husain, A.R.; Danapalasingam, K.A. Intelligent adaptive backstepping control for MIMO uncertain non-linear quadrotor helicopeter systems. *Trans. Inst. Meas. Contr.* **2015**, *37*, 345–361. [CrossRef]

23.　Zhou, L.; Zhang, J.; Dou, J.; Wen, B. A fuzzy adaptive backstepping control based on mass observer for trajectory tracking of a quadrotor UAV. *Int. J. Adapt. Signal Process.* **2018**, *32*, 1675–1693. [CrossRef]

24.　Su, Y.X.; Zheng, C.H.; Sun, D.; Duan, B.Y. A simple nonlinear velocity estimator for high-performance motion control. *IEEE Trans. Ind. Electr.* **2005**, *52*, 1161–1169. [CrossRef]

25.　Guo, B.Z.; Zhao, Z.L. On convergence of tracking differentiator. *Int. J. Control* **2011**, *84*, 693–701. [CrossRef]

26.　Bu, X.W.; Wu, X.Y.; Zhang, R.; Ma, Z.; Huang, J. Tracking differentiator design for the robust backstepping control of flexible air-breathing hypersonic vehicle. *J. Frankl. Inst.* **2015**, *352*, 1739–1765. [CrossRef]

27.　Yang, Z.; Ji, J.; Sun, J.; Zhu, H.; Zhao, Q. Active disturbance rejection control for backstepping induction motor based on hyperbolic tangent tracking differentiator. *IEEE J. Emerg. Sel. Top. Power Electr.* **2020**, *8*, 2623–2633. [CrossRef]

28.　Zong, X.; Chen, Z.; Zheng, J.; Cheng, X. Design of a rapid tangent sigmoid function tracking differentiator 2020. In Proceedings of the IEEE 4th ITNEC 2020, Chongqing, China, 12–14 June 2020; pp. 15–19.

29.　Zhou, W.; Xu, H.; Zong, X. Research on tracking system of optoelectronic pod based on a rapid tangent sigmoid function tracking differentiator. In Proceedings of the IEEE 5th ITNEC 2021, Xi'an, China, 15–17 October 2021; pp. 217–221.

30.　Levant, A. Robust exact differentiation via sliding mode technique. *Automatica* **1998**, *34*, 379–384. [CrossRef]

31.　Levant, L. Higher-order sliding modes, differentiation and output-feedback control. *Int. J. Control* **2003**, *76*, 9–10. [CrossRef]

32.　Zhang, J.; Xia, J.; Sun, W.; Wang, Z.; Shen, H. Command filter-based finite-time adaptive fuzzy control for nonlinear systems with uncertain disturbance. *J. Frankl. Inst.* **2019**, *356*, 11270–11284. [CrossRef]

33.　Zhao, L.; Yu, J.; Shi, P. Command filtered backstepping-based attitude containment control for spacecraft formation. *IEEE Trans. Syst. Man Cyber. Syst.* **2021**, *51*, 1278–1287. [CrossRef]

34.　Slotine, J.J.; Li, W. *Applied Nonlinear Control*; Prentice-Hall: New York, NY, USA, 1991.

35.　Lu, C.; Hwang, Y.; Shen, Y. Backstepping sliding mode tracking control of a vane-type air motor X-Y table motion system. *ISA Trans.* **2011**, *50*, 278–286. [CrossRef]

36.　Chen, N.; Song, F.; Li, G.; Sun, X.; Ai, C. An adaptive sliding mode backstepping control for the mobile manipulator with holonomic constraints. *Commun. Nonlinear Sci. Numer. Simulat.* **2013**, *18*, 2885–2899. [CrossRef]

37.　Haitao, W.; Xinmin, D.; Jianping, X.; Jiaolong, L. Dynamic modeling of a hose-drogue aerial refueling system and integral sliding mode backstepping control for the hose whipping phenomenon. *Chin. J. Aeronaut.* **2014**, *27*, 930–946.

38.　Song, Z.; Sun, K. Adaptive backstepping sliding mode control with fuzzy monitering strategy for a kind of mechanical system. *ISA Trans.* **2014**, *53*, 125–133. [CrossRef] [PubMed]

39.　Chen, W.H.; Balance, D.J.; Gawthrop, P.J.; O'Reilly, J. A nonlinear disturbance observer for robotic manipulator. *IEEE Trans. Ind. Electr.* **2000**, *47*, 932–938. [CrossRef]

40. Yang, J.; Chen, W.H.; Li, S. Nonlinear disturbance observer based robust control for systems with mismatched disturbances/uncertainties. *IET Control. Theory Appl.* **2011**, *5*, 2053–2062. [CrossRef]

41. Han, J. From PID to active disturbance rejection control. *IEEE Trans. Ind. Electr.* **2009**, *56*, 900–906. [CrossRef]

42. Li, S.; Yang, J.; Chen, H.; Chen, X. Generalized extended state observer based control for systems with mismatched uncertainties. *IEEE Trans. Ind. Electr.* **2012**, *59*, 4792–4802. [CrossRef]

43. Moreno, J.A.; Osorio, M. A Lyapunov approach to second-order sliding mode controller and observers. In Proceedings of the 2008 47th IEEE Conference on Decision and Control, Cancun, Mexico, 9–11 December 2008; Volume 53, pp. 2856–2861.

44. Yang, J.; Li, S.; Sun, L. Nonlinear-disturbance-observer-based robust flight control for airbreathing hypersonic vehicles. *IEEE Trans. Aerosp. Electron. Syst.* **2013**, *49*, 1263–1274. [CrossRef]

45. Bu, X.W.; Wu, X.Y.; Chen, Y.X.; Bai, R.Y. Design of a class of new nonlinear disturbance observers based on tracking differentiators for uncertain dynamic systems. *Int. J. Control. Autom. Syst.* **2015**, *13*, 595–602. [CrossRef]

46. Perez-Ventura, U.; Fridman, L. Design of super-twisting control gains: A describing function based methodology. *Automatica* **2019**, *99*, 175–180. [CrossRef]

47. Moreno, J.A.; Osorio, M. Strict Lyapunov functions for the supertwisting algorithm. *IEEE Trans. Autom. Control* **2012**, *57*, 1035–1040. [CrossRef]

48. Gonzalez, T.; Moreno, J.; Fridman, L. Variable gain super-twisting sliding mode control. *IEEE Trans. Autom. Control* **2012**, *57*, 2100–2105. [CrossRef]

49. Shtessel, Y.; Taleb, M.; Plestan, F. A novel adaptive-gain supertwisting sliding mode controller: Methodology and application. *Automatica* **2012**, *48*, 759–769. [CrossRef]

50. Yu, J.; Shi, P.; Zhao, L. Finite-time command filtered backstepping control for a class of nonlinear systems. *Automatica* **2018**, *92*, 173–180. [CrossRef]

51. Bucolo, M.; Buscarino, A.; Fortuna, L.; Gagliano, S. Bifurcation scenarios for pilot induced scillations. *Aerosp. Sci. Technol.* **2020**, *106*, 106194. [CrossRef]